

**1 Local wind regime induced by giant linear dunes:
2 comparison of ERA5-Land reanalysis with surface
3 measurements**

**4 Cyril Gadal · Pauline Delorme ·
5 Clément Narteau · Giles F.S. Wiggs ·
6 Matthew Baddock · Joanna M. Nield ·
7 Philippe Claudin**

8
9 Received: DD Month YEAR / Accepted: DD Month YEAR

10 Abstract

11 Emergence and growth of sand dunes results from the dynamic interaction
12 between topography, wind flow and sediment transport. While feedbacks be-
13 tween these variables are well studied at the scale of a single and relatively
14 small dune, the average effect of a periodic large-scale dune pattern on atmo-
15 spheric flows remains poorly constrained, due to a lack of data in major sand
16 seas. Here, we compare local measurements of surface winds to the predictions
17 of the ERA5-Land climate reanalysis at four locations in Namibia, within and
18 outside the giant linear dune field of the Namib sand sea. In the desert plains
19 to the north of the sand sea, observations and predictions agree well. This
20 is also the case in the interdune areas of the sand sea during the day. Dur-
21 ing the night, however, an additional wind component aligned with the giant
22 dune orientation is measured, in contrast to the easterly wind predicted by

C. Gadal

Institut de Mécanique des Fluides de Toulouse, Université de Toulouse Paul Sabatier, CNRS,
Toulouse INP-ENSEEIHT, Toulouse, France. E-mail: cyril.gadal@imft.fr

P. Delorme

Energy and Environment Institute, University of Hull, Hull, UK.

C. Narteau

Institut de Physique du Globe de Paris, Université de Paris, CNRS, Paris, France.

G. Wiggs

School of Geography and the Environment, University of Oxford, Oxford, UK.

M. Baddock

Geography and Environment, Loughborough University, Loughborough, UK.

J.M. Nield

School of Geography and Environmental Science, University of Southampton, Southampton,
UK.

P. Claudin

Physique et Mécanique des Milieux Hétérogènes, CNRS, ESPCI Paris, PSL Research Uni-
versity, Université de Paris, Sorbonne Université, Paris, France.

the ERA5-Land reanalysis. We link these discrepancies, with wind deviation and velocity attenuation larger than 50° and 60 %, to the daily cycle of the turbulent atmospheric boundary layer over a complex topography, and to the associated flow regimes. During the night, a shallow boundary layer induces a flow confinement associated with a strong streamline compression above the giant dunes, resulting in large flow deviations, especially for the lower winds. During the day, the flow confinement is reduced by a thicker boundary layer and higher wind velocities, and the feedback of the giant dunes on the atmospheric flow is negligible. We finally propose that this mechanism and the resulting wind deflections by the giant dunes could explain the occurrence of smaller-scale secondary dune patterns, elongating along a different orientation compared to the primary dunes between which they develop.

Keywords Atmospheric boundary layer · Sand dunes · Flow over hills

36 1 Introduction

37 The description of turbulent flows over complex topography is relevant for
38 a large variety of different environmental systems (Sherman 1978; Walmsley
39 et al. 1982; Baines 1995; Wood 2000; Venditti et al. 2013; Finnigan et al.
40 2020). For example, the flow over hills is of primary interest for wind power,
41 meteorological and air pollution phenomena (Taylor et al. 1987). The proper-
42 ties of these flows are also key to the understanding of geophysical phenom-
43 ena, including the formation of wind-driven waves on the ocean surface (Sulli-
44 van and McWilliams 2010), dissolution bedforms (Claudin et al. 2017; Guérin
45 et al. 2020), or sedimentary ripples and dunes (Bagnold 1941; Charru et al.
46 2013; Courrech du Pont 2015). Importantly, the troposphere presents a vertical
47 structure, with a lower convective boundary layer, of typical kilometer-scale
48 thickness, capped by a stably stratified region (Stull 1988). The largest topo-
49 graphic obstacles, such as mountains, can therefore interact with this upper
50 region and lead to internal wave generation or significant wind disturbances,
51 such as lee-side downslope winds (Durran 1990).

52 Compared to hills and mountains, aeolian sand dunes offer idealized ele-
53 vation profiles for the study of atmospheric turbulent flow over topographies,
54 due to their smooth shape, free of canopies. Besides, dunes provide a rather
55 wide range of scales, from decameters to kilometers, and very often come in
56 a fairly regular pattern, which further simplifies the flow structure analysis.
57 Past studies have highlighted two important topographic feedbacks on the
58 wind flow close to the dune/hill surface. First is the effect on wind speed, with
59 documented flow acceleration on upwind slopes (Weaver and Wiggs 2011) and
60 deceleration on downwind slopes (Baddock et al. 2007), where the speed-up
61 factor is essentially proportional to the obstacle aspect ratio (Jackson and
62 Hunt 1975). Importantly, the velocity maximum is typically shifted upwind
63 of the obstacle crest (Jackson and Hunt 1975; Claudin et al. 2013). This be-
64 haviour has been theoretically predicted by means of asymptotic analysis of
65 a neutrally stratified boundary-layer flow over an obstacle of vanishing as-
66 pect ratio (Jackson and Hunt 1975; Mason and Sykes 1979; Sykes 1980; Hunt
67 et al. 1988; Belcher and J.C.R. 1998; Kroy et al. 2002). Experiments in flumes
68 (Zilker et al. 1977; Zilker and Hanratty 1979; Frederick and Hanratty 1988;
69 Poggi et al. 2007; Bristow et al. 2022), in wind tunnels (Gong and Ibbetson
70 1989; Finnigan et al. 1990; Gong et al. 1996) and in field conditions at all
71 scales (Taylor and Teunissen 1987; Claudin et al. 2013; Fernando et al. 2019;
72 Lü et al. 2021), have also documented this effect. Interestingly, a similar be-
73 haviour exists for the pressure perturbation, but with a slight downwind shift
74 for the pressure minimum (Claudin et al. 2021). The second effect, much less
75 studied, is the flow deflection that occurs when the incident wind direction is
76 not perpendicular to the ridge crest. While predicted to be small (less than
77 10°) in the linear regime valid for shallow topography (Gadal et al. 2019),
78 significant flow steering has been reported in the field on the downwind side of
79 steep enough obstacles, such as well-developed sand dunes (Tsoar and Yaalon
80 1983; Sweet and Kocurek 1990; Walker and Nickling 2002; Smith et al. 2017)

and in particular coastal foredunes (e.g. Hunter et al. (1983), Rasmussen (1989), Walker et al. (2006), Walker et al. (2009), Hesp et al. (2015), Walker et al. (2017), de Winter et al. (2020)), mountain ranges (Kim et al. 2000; Lewis et al. 2008; Fernando et al. 2019), and valley topographies (Wiggs et al. 2002; Garvey et al. 2005).

Wind measurements over sand dunes has been mainly performed over small bedforms, typically a few meters high (corresponding to several tens of meters long) (e.g. Mulligan (1988), Hesp et al. (1989), Lancaster et al. (1996), Mckenna Neuman et al. (1997), Sauermann et al. (2003), Andreotti et al. (2002), Walker and Nickling (2002), Weaver and Wiggs (2011)). For practical reasons, fewer studies performed similar measurements on giant dunes (Havholm and Kocurek 1988), with kilometer-scale wavelengths and heights of tens of meters. However, such large dunes provide a choice configuration for the study of turbulent flows over a complex topography. First, one expects larger wind disturbances for larger obstacles. Secondly, their large size can make them interact with the vertical structure of the atmosphere (Andreotti et al. 2009). Third, they usually form large patterns in sand seas and thus behave as rather clean periodic perturbations, in contrast with isolated dunes. Finally, because the morphodynamics of aeolian bedforms is strongly dependent on the local wind regime (Livingstone and Warren 2019), one can expect to see the consequences of windflow disturbance by large dunes on neighbouring small dunes (Brookfield 1977; Ewing et al. 2006). A similar effect is observed on the properties of impact ripple patterns due to the presence of dunes (Howard 1977; Hood et al. 2021).

Atmospheric flows have been much studied at the desert-scale with climate reanalyses based on global atmospheric models (Blumberg and Greeley 1996; Livingstone et al. 2010; Ashkenazy et al. 2012; Jolivet et al. 2021; Hu et al. 2021; Gunn et al. 2021b), such as ERA-40, ERA-Interim or ERA5 (Uppala et al. 2005; Dee et al. 2011; Hersbach et al. 2020). However, the spatial resolution of these reanalyses (tens of kilometers) implies average quantities that do not resolve the smaller scales of interest, which range from individual dunes to small mountains (Livingstone et al. 2010). Recently, the release of ERA5-Land has partly resolved this limitation by providing up to 70 years of hourly wind predictions at a 9 km spatial resolution (Muñoz-Sabater et al. 2021). However, its validity remains to be studied, especially in remote desert areas where assimilation of measured data is very low.

In this work, we compare local wind speeds and directions measured by meteorological stations at four different locations inside and north of the giant linear dune field of the Namib sand sea to the regional predictions of the ERA5-Land climate reanalysis. Where the meteorological stations are surrounded by a relatively flat environment, we show that local measurements and regional predictions agree well. The agreement is also good in the interdune areas of the sand sea, except for some weak winds blowing at night, which exhibit an additional component aligned with the giant dune orientation. These winds are not predicted by the ERA5-Land reanalysis (section 2). Further, we are able to link the magnitude of these differences to the circadian cycle of the

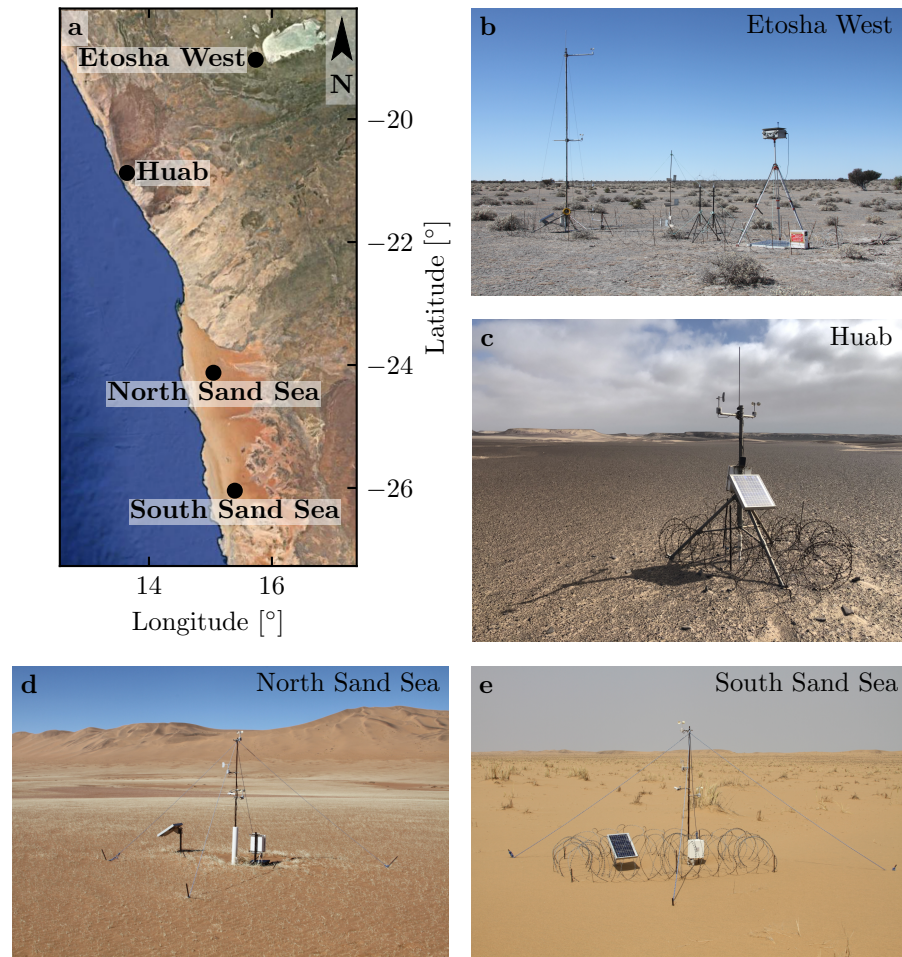


Fig. 1 Studied field sites. **a:** Location of the different sites in Namibia. **b–e:** Photographs of the meteorological stations.

atmospheric boundary layer (section 3). Finally, we draw implications for the wind disturbances on smaller-scale dunes (section 4), suggesting a possible origin for crossing dunes.

2 Wind regimes across the Namib Sand Sea

We measured the wind regime at four different locations in Namibia, representative of various arid environments across the Namib desert (Fig. 1, Fig. 2). The Etosha West station was located at the Adamax waterhole to the west of Etosha Pan in northern Namibia, in a sparsely vegetated area. The Huab station was near the coast on a hyper-arid flat gravel plain lying north the

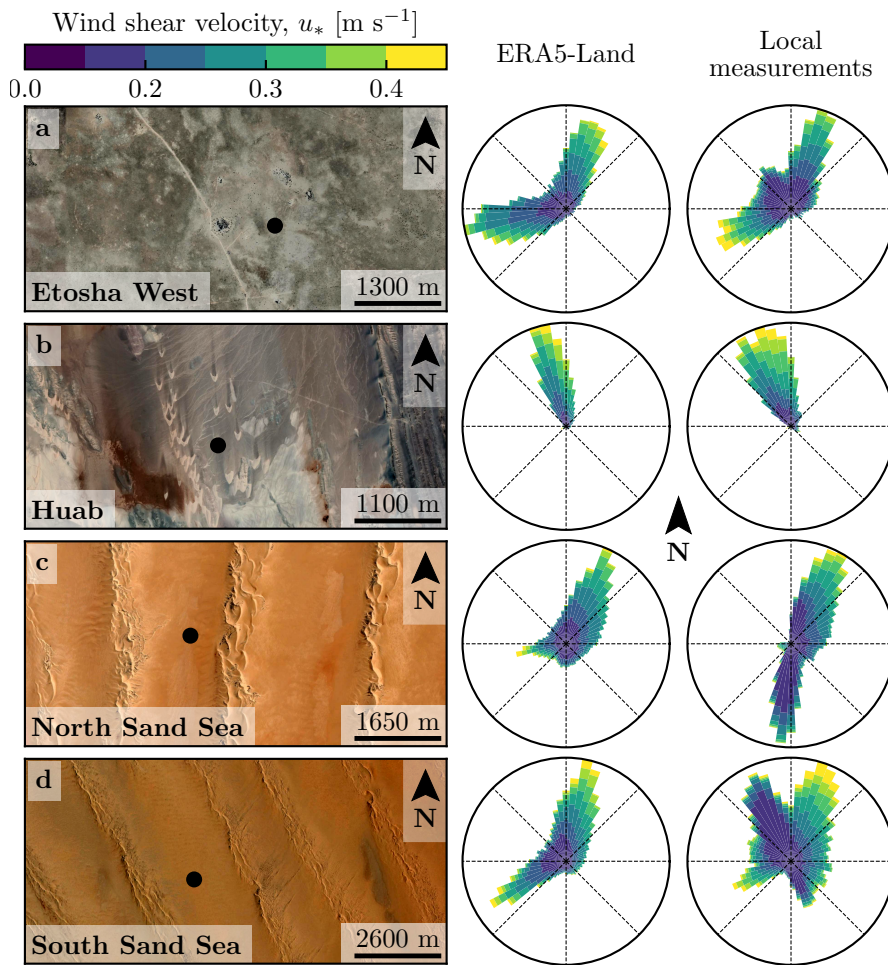


Fig. 2 Wind data used in this study. Satellite images of the different environments (Google-Earth, Maxar Technologies, CNES/Airbus) are shown on the left. The black dots show the location of the wind measurements stations. On the right of the photos, the corresponding wind roses representing the data from the ERA5-Land climate reanalysis and the local wind stations are displayed. Note: the graphical convention for the wind roses is that the bars show the direction towards which the wind blows (see color bar for velocity scale).

136 ephemeral Huab river. Here, barchan dunes up to a few meters in height de-
 137 velop from the sediment blowing out of the river valley (Nield et al. 2017;
 138 Hesp and Hastings 1998). These two stations were both located in relatively
 139 flat environments. In contrast, the North Sand Sea and South Sand Sea sta-
 140 tions were located in the interdunes between linear dunes with kilometer-scale
 141 wavelengths, hectometer-scale heights and superimposed patterns. In this sec-
 142 tion, we describe and compare winds from local measurements and climate
 143 reanalysis predictions.

144 2.1 Wind and elevation data

145 At each meteorological station (Fig. 1), wind speed and direction were sampled
146 every 10 minutes using cup anemometers (Vector Instruments A100-LK) and
147 wind vanes (Vector Instruments W200-P) at a single height, which was between
148 2 m and 3 m depending on the station. The available period of measurements at
149 each station ranged from 1 to 5 discontinuous years distributed between 2012
150 and 2020 (Online Resource Fig. S1). We checked that at least one complete
151 seasonal cycle was available for each station. Regional winds were extracted
152 at the same locations and periods from the ERA5-Land dataset, which is a
153 replay at a smaller spatial resolution of ERA5, the latest climate reanalysis
154 from the ECMWF (Hersbach et al. 2020; Muñoz-Sabater et al. 2021). This
155 dataset provided hourly predictions of the 10-m wind velocity and direction
156 at a spatial resolution of $0.1^\circ \times 0.1^\circ$ (≈ 9 km in Namibia).

157 To enable direct comparison, the local wind measurements were averaged
158 into 1-hr bins centered on the temporal scale of the ERA5-Land estimates
159 (Online Resource Fig. S2). As the wind velocities of both datasets were pro-
160 vided at different heights, we converted them into shear velocities u_* (Online
161 Resource section 1), characteristic of the turbulent wind profile. Wind roses
162 in Fig. 2 show the resulting wind data.

163 Dune properties were computed using autocorrelation on the 30-m Digital
164 Elevation Models (DEMs) of the shuttle radar topography mission (Farr et al.
165 2007). For the North and South Sand Sea stations, we obtain, respectively,
166 orientations of 85° and 125° with respect to the North, wavelengths of 2.6 km
167 and 2.3 km and amplitudes (or half-heights) of 45 m and 20 m (Online Resource
168 Fig. S4 for more details). This agrees with direct measurements made on site.

169 2.2 Comparison of local and regional winds

170 The measured and predicted wind regimes are shown in Fig. 2. In the Namib,
171 the regional wind patterns are essentially controlled by the sea breeze, result-
172 ing in strong northward components (sometimes slightly deviated by the large
173 scale topography) present in all regional wind roses (Lancaster 1985). These
174 daytime winds are dominant during the period October-March (Fig. 3f and
175 Online Resource Fig. 4f). During April-September, an additional (and often
176 nocturnal) easterly component can also be recorded, induced by the combina-
177 tion of katabatic winds forming in the mountains, and infrequent ‘berg’ winds,
178 which are responsible for the high wind velocities observed (Lancaster et al.
179 1984). The frequency of these easterly components decreases from inland to
180 the coast. As a result, bidirectional wind regimes within the Namib Sand Sea
181 and at the west Etosha site (Fig. 2a,c,d) and a unidirectional wind regime on
182 the coast at the outlet of the Huab River (Fig. 2b) are observed.

183 In the case of the Etosha West and Huab stations, the time series of wind
184 speed and direction from the regional predictions quantitatively match those
185 corresponding to the local measurements (Figs. 3, 4 and Online Resource

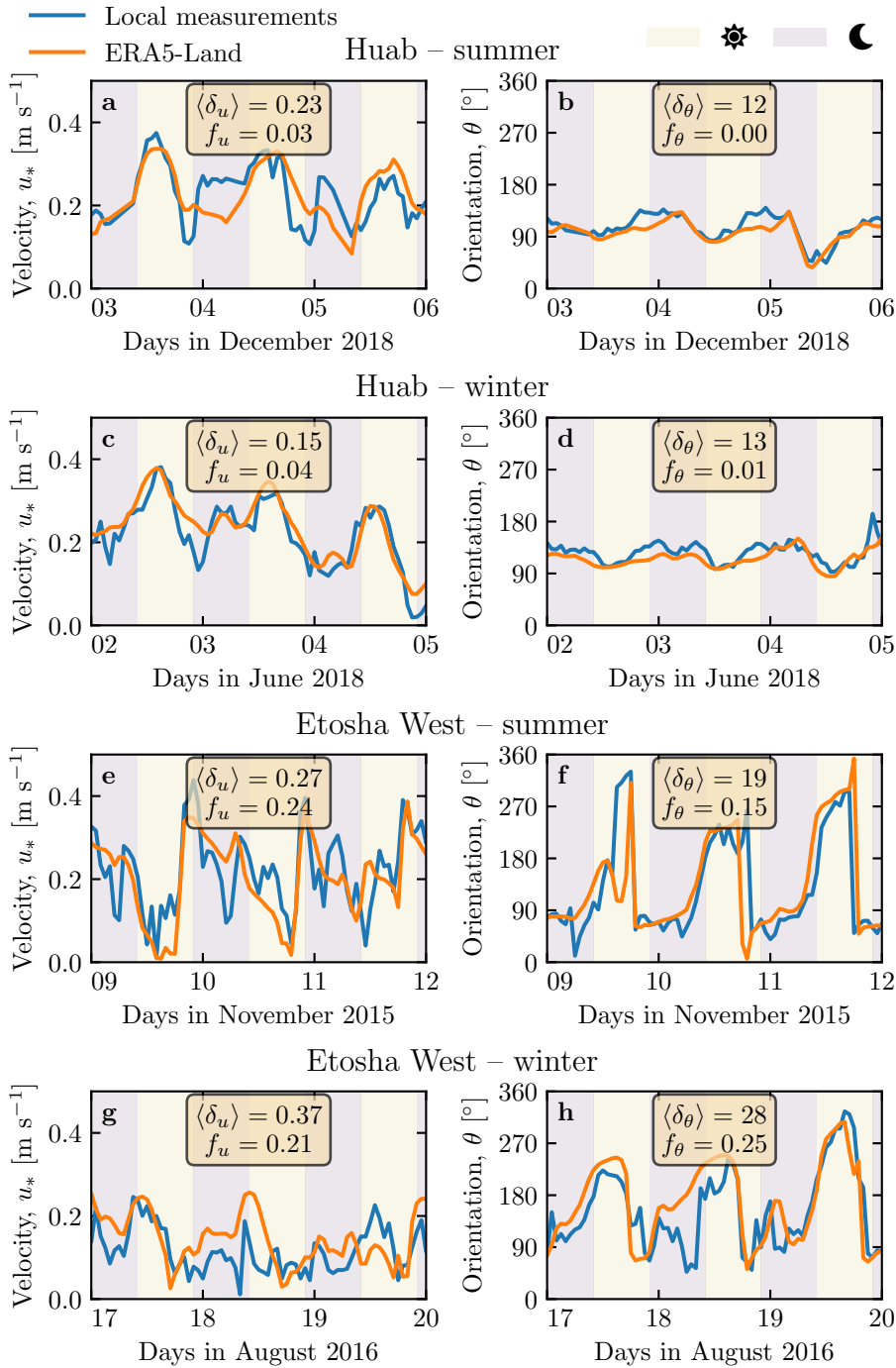


Fig. 3 Temporal comparison between the wind data coming from the ERA5-Land climate reanalysis (orange lines) and from the local measurements (blue lines). Coloured swathes indicate day (between 10.00 UTC and 22.00 UTC) and night (before 10.00 UTC or after 22.00 UTC). Numbers in legends indicate the average flow deflection δ_θ and relative wind modulation δ_u over the displayed period (see section 3.2 for their definitions), as well as the percentage f_θ and f_u of occurrence of extreme events ($\delta_\theta > 50^\circ$, $|\delta_u| > 0.6$). **a–b:** Huab station in summer. **b–c:** Huab station in winter. **d–e:** Etosha West station in summer. **f–g:** Etosha West station in winter. Time series of the two other stations are shown in Fig. 5.

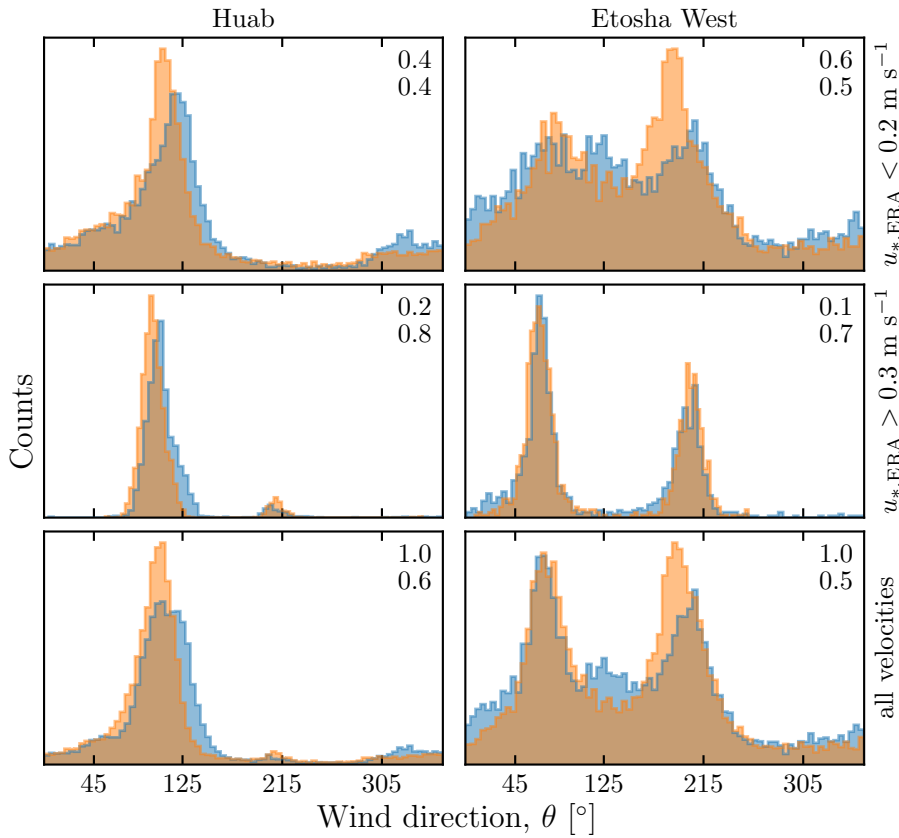


Fig. 4 Distributions of wind direction at Huab and Etosha West stations for the ERA5-Land climate reanalysis (orange) and the local measurements (blue). In each subplot, both distributions are plotted from the same time steps, selected for different ranges of the wind wind velocity (rows) in the ERA5-Land dataset. The numbers at the upper right corners give the percentage of time steps selected in each sub-range (top), as well as the percentage of them corresponding to the day – defined between 10.00 UTC and 22.00 UTC (bottom).

186 Fig. S5). For the North Sand Sea and South Sand Sea stations within the giant
 187 linear dune field, we observe that this agreement is also good, but limited to the
 188 October-March time period (Fig. 4a, b, e, f). However, the field-measured wind
 189 roses exhibit additional wind components aligned with the dune orientation,
 190 as evidenced on the satellite images (Fig. 2c,d).

191 More precisely, during the April-September period, the local and regional
 192 winds in the interdune match during daytime only, i.e when the southerly/southwesterly
 193 sea breeze dominates (Figs. 5c,d,g,h and 6). In the late afternoon and during
 194 the night, when the easterly ‘berg’ and katabatic winds blow, measurements
 195 and predictions differ. In this case, the angular wind distribution of the lo-
 196 cal measurements exhibits two additional modes corresponding to reversing
 197 winds aligned with the dune orientation (purple frame in Fig. 6, Online Re-
 198 source Fig. S6). This deviation is also associated with a general attenuation

of the wind strength (Online Resource Fig. S7). Remarkably, all these figures show that these wind reorientation and attenuation processes occur only at low velocities of the regional wind, typically for $u_*^{\text{ERA5-Land}} \lesssim 0.2 \text{ m s}^{-1}$. For shear velocities larger than $u_*^{\text{ERA5-Land}} \simeq 0.3 \text{ m s}^{-1}$, the wind reorientation is not apparent. Finally, for intermediate shear velocities, both situations of wind flow reoriented along the dune crest and not reoriented can be successively observed (Online Resource Fig. S6). Importantly, these values are not precise thresholds (and certainly not related to the threshold for sediment transport), but indicative of a crossover between regimes, whose physical interpretation is discussed in the next section.

3 Influence of wind speed and circadian cycle on the atmospheric boundary layer

The wind deflection induced by dunes has previously been related to the incident angle between wind direction and crest orientation, with a maximum deflection evident for incident angles between 30° and 70° (Walker et al. 2009; Hesp et al. 2015). In the data analysed here, the most deflected wind at both the North and South Sand Sea stations is seen to be where the incident angle is perpendicular to the giant dunes (Figs. 2 and 6). It therefore appears that in our case, the incident wind angle is not the dominant control on maximum wind deflection. Further, and as shown in Fig. 6, winds of high and low velocities show contrasting behaviour in characteristics of deflection. This suggests a change in hydrodynamical regime between the winds. In this section, we discuss the relevant parameters associated with the dynamical mechanisms that govern the interactions between the atmospheric boundary layer flow and giant dune topographies. This analysis allows us to provide a physics-based interpretation of our measured wind data.

3.1 Flow over a modulated bed

Taking as a reference the turbulent flow over a flat bed, the general framework of our study is understanding and describing the flow response to a bed modulation (e.g. a giant dune). Without loss of generality, we can consider in this context an idealised bed elevation in the form of parallel sinusoidal ridges, with wavelength λ (or wavenumber $k = 2\pi/\lambda$) and amplitude ξ_0 , and where the reference flow direction makes a given incident angle with respect to the ridge crest (Andreotti et al. 2012). Part of this response, on which we focus here, is the flow deflection by the ridges. In a simplified way, it can be understood from the Bernoulli principle (Hesp et al. 2015): as the flow approaches the ridge crest, the compression of the streamlines results in larger flow velocities, and thus lower pressures (Jackson and Hunt 1975). An incident flow oblique to the ridge is then deflected towards lower pressure zones, i.e towards the crest. Turbulent dissipation tends to increase this effect downstream, resulting in wind deflection along the crest in the lee side (Gadal et al. 2019).

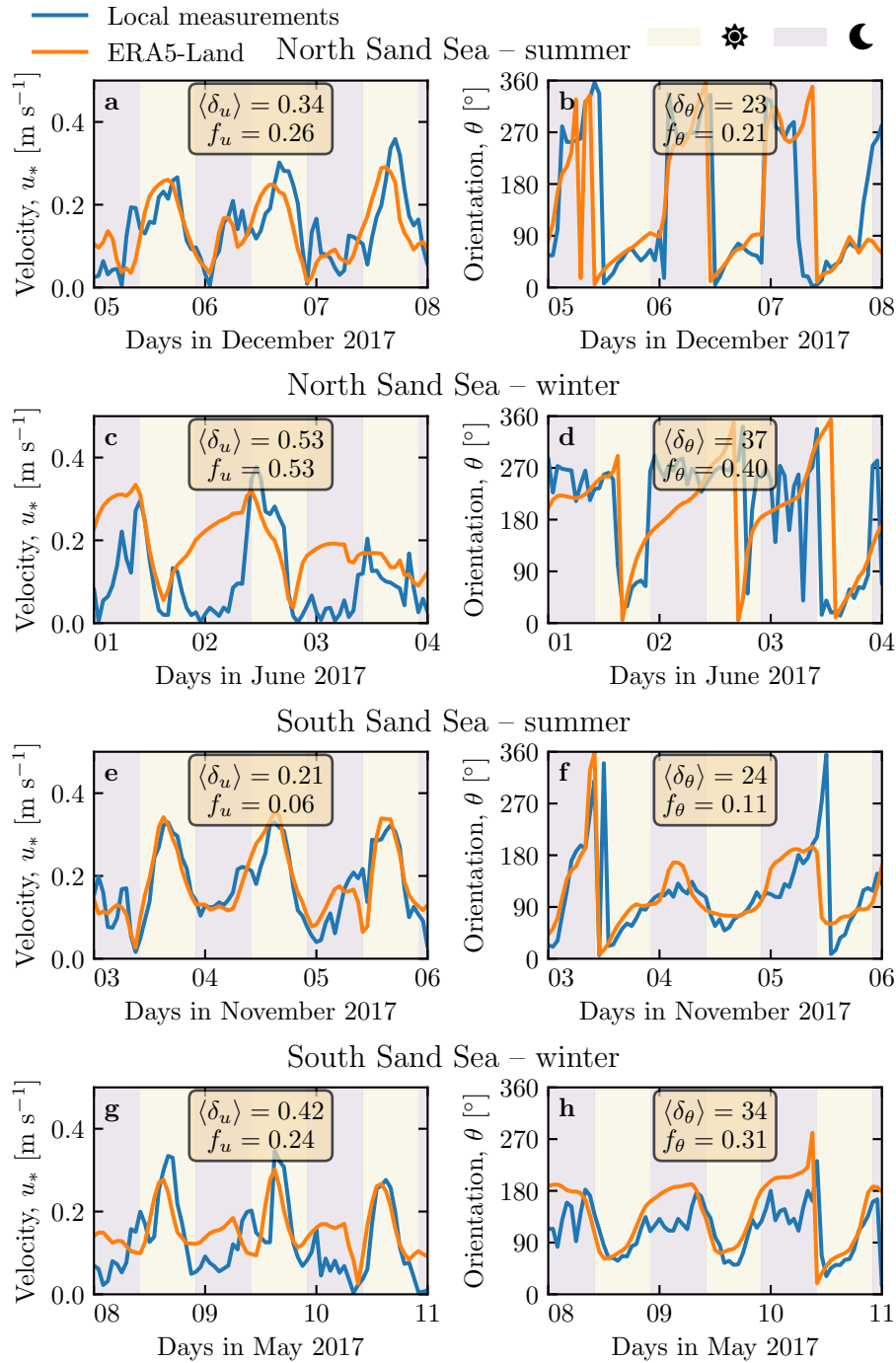


Fig. 5 Same as Fig. 3 for North Sand Sea station in summer (a–b), North Sand Sea station in winter (b–c), South Sand Sea station in summer (d–e) and South Sand Sea station in winter (f–g).

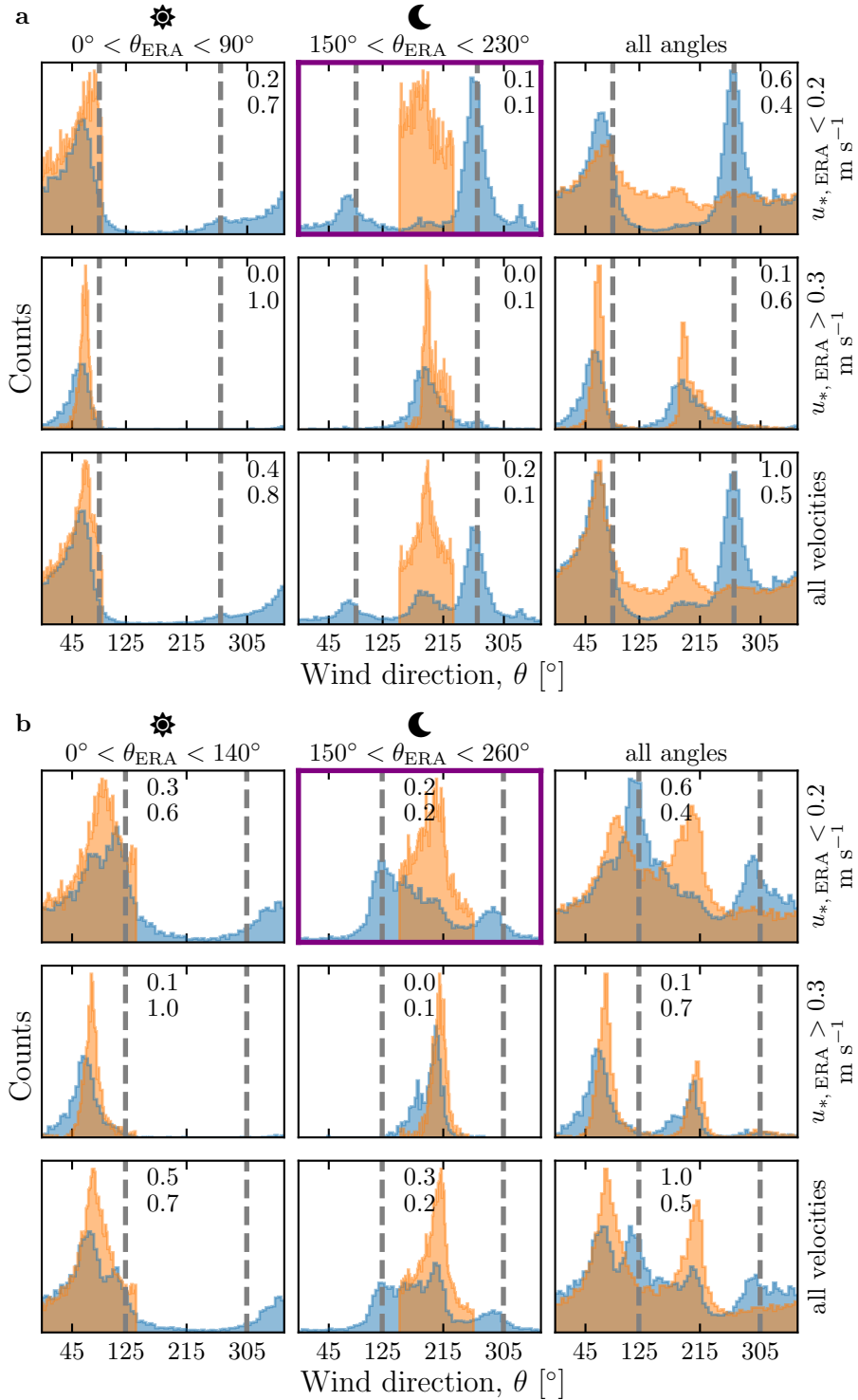


Fig. 6 Same as Fig. 4 but for North Sand Sea (**a**) and South Sand Sea (**b**) stations. Here, subplots correspond to different ranges for the wind direction (columns) and wind velocity (rows) of the ERA5-Land dataset. The grey vertical dashed lines indicate the main dune orientation. In contrast with observations at the Huab and Etosha West stations (Fig. 4), histograms do not match well at low wind velocities, and the purple frame highlights the regime (low wind velocities, nocturnal easterly wind) in which the data from both datasets differ most.

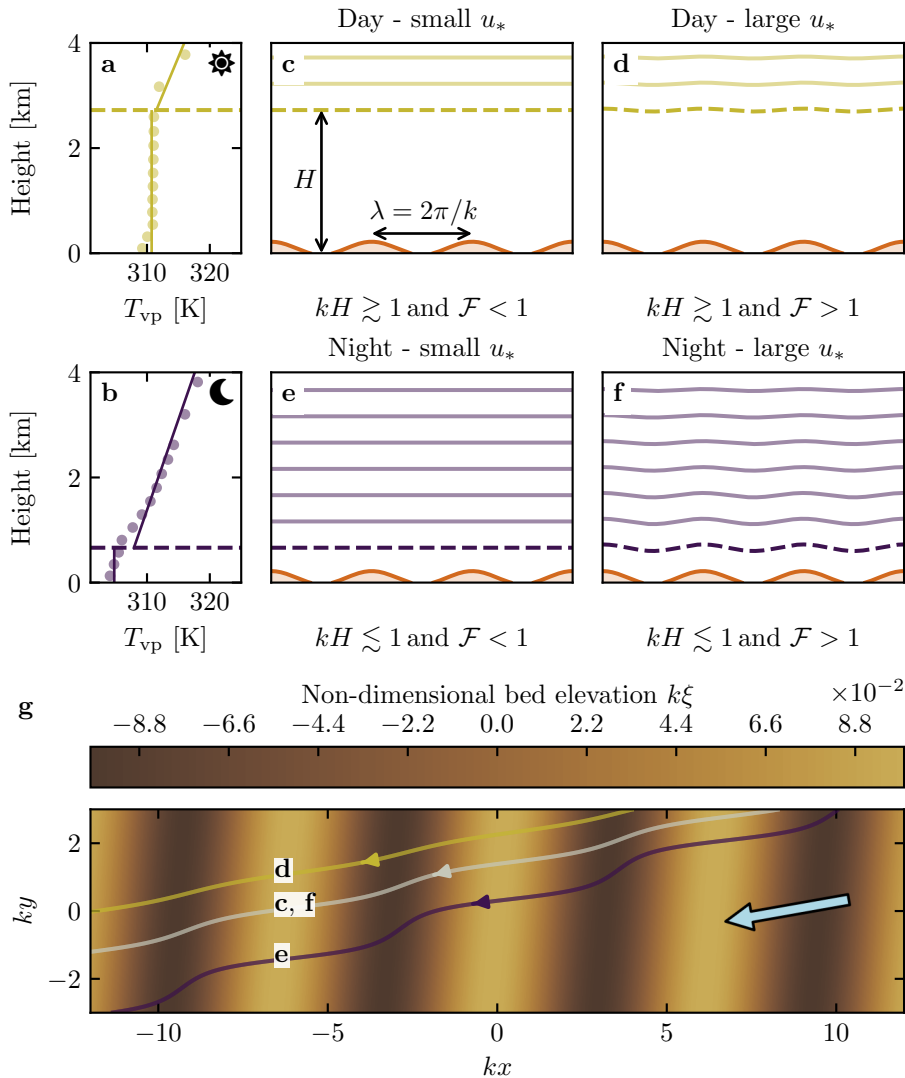


Fig. 7 **a–b:** Vertical profiles of the virtual potential temperature T_{vp} at two different time steps (day - 03/11/2015 - 12.00 UTC, night - 01/13/2013 - 09.00 UTC) at the North Sand Sea station. Dots: data from the ERA5 reanalysis. Dashed lines: boundary layer height given by the ERA5 reanalysis (Online Resource section 2). Plain lines: vertical (boundary layer) and linear (free atmosphere) fits to estimate the stratification properties. **c–f:** Sketches representing the interaction between the giant dunes and the atmospheric flow for different meteorological conditions. **g:** Streamlines over a sinusoidal topography $\xi(x, y)$ qualitatively representing the effect of low, medium and strong flow confinement, in relation to the above panels (see Appendix 1 for more details). The blue arrow indicates the undisturbed wind direction.

Flow confinement below a capping surface, which enhances streamline compression, has a strong effect on the hydrodynamic response and typically increases flow deflection. This is the case for bedforms forming in open channel flows such as rivers (Kennedy 1963; Chang and Simons 1970; Mizumura 1995; Colombini 2004; Fourrière et al. 2010; Andreotti et al. 2012; Unsworth et al. 2018). This is also relevant for aeolian dunes as they evolve in the turbulent atmospheric boundary layer (ABL) capped by the stratified free atmosphere (FA) (Andreotti et al. 2009). Two main mechanisms, associated with dimensionless numbers must then be considered (Fig. 7). First, topographic obstacles typically disturb the flow over a characteristic height similar to their length. As flow confinement is characterised by a thickness H , the interaction between the dunes and the wind in the ABL is well captured by the parameter kH . The height H is directly related to the sensitive heat flux from the Earth surface. It is typically on the order of a kilometre, but significantly varies with the circadian and seasonal cycles. Emerging and small dunes, with wavelengths in the range 20 to 100 m, are not affected by the flow confinement, corresponding to $kH \gg 1$. For giant dunes with kilometer-scale wavelengths, however, their interaction with the FA can be significant (Andreotti et al. 2009). This translates into a parameter kH in the range 0.02–5, depending on the moment of the day and the season. A second important mechanism is associated with the existence of a thin intermediate so-called capping layer between the ABL and the FA. It is characterised by a density jump $\Delta\rho$, which controls the ‘rigidity’ of this interface, i.e. how much its deformation affects streamline compression. This is usually quantified using the Froude number (Vosper 2004; Stull 2006; Sheridan and Vosper 2006; Hunt et al. 2006; Jiang 2014):

$$\mathcal{F} = \frac{U}{\sqrt{\frac{\Delta\rho}{\rho_0} g H}}, \quad (1)$$

where U is the wind velocity at the top of the ABL and ρ_0 its average density. The intensity of the stratification, i.e. the amplitude of the gradient $|\partial_z \rho|$ in the FA, also impacts the ability to deform the capping layer under the presence of an underlying obstacle, and thus affects the influence of flow confinement. This can be quantified using the internal Froude number (Vosper 2004; Stull 2006; Sheridan and Vosper 2006; Hunt et al. 2006; Jiang 2014) $\mathcal{F}_I = kU/N$, where $N = \sqrt{-g\partial_z \rho/\rho_0}$ is the Brunt-Väisälä frequency (Stull 1988). Both Froude numbers have in practice the same qualitative effect on flow confinement (a smaller Froude corresponding to a stiffer interface), and we shall restrict the main discussion to \mathcal{F} only.

With this theoretical framework in mind, and in the context of the measured wind data in the North and South Sand Sea stations, the smallest wind disturbances are expected to occur during the day, when the ABL depth is the largest and comparable to the dune wavelength ($kH \gtrsim 1$), which corresponds to a weak confinement situation (Fig. 7c,d). In contrast, large wind disturbances are expected to occur during the night, when the confinement

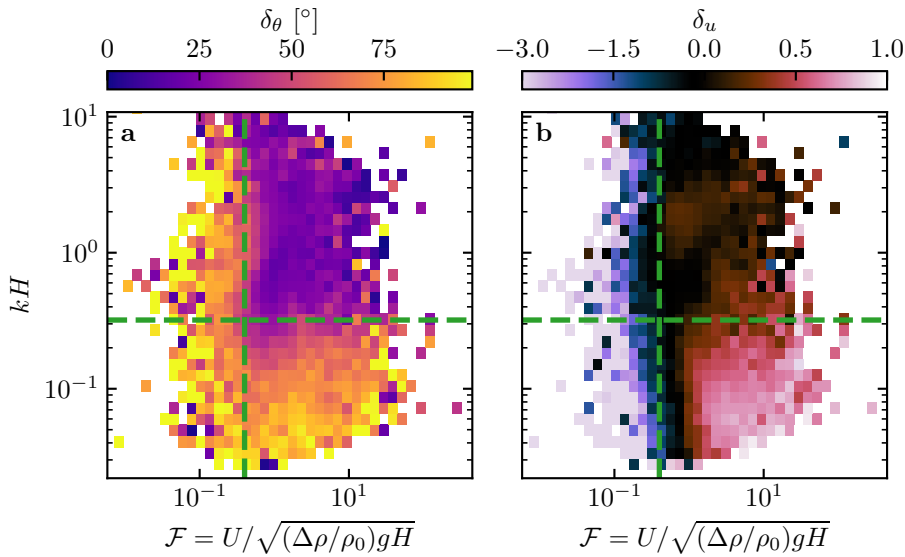


Fig. 8 Regime diagrams of the wind deviation δ_θ (a) and relative attenuation/amplification δ_u (b) in the space (\mathcal{F}, kH) , containing the data from both the North Sand Sea and South Sand Sea stations. The green dashed lines empirically delimit the different regimes. The point density in each bin of the diagrams is shown in Online Resource Fig. S10 – 95% of the data occur in the range $-1 < \delta u < 1$. Similar regime diagrams in the spaces (\mathcal{F}_I, kH) and $(\mathcal{F}_I, \mathcal{F})$ are shown in Online Resource Fig. S11.

281 is mainly induced by a shallow ABL (Fig. 7e). However, this strong confinement
 282 can be somewhat reduced in the case of strong winds, corresponding to
 283 large values of the Froude number and a less ‘rigid’ interface (Fig. 7f). This
 284 is in qualitative agreement with the transition from deflected to non-deflected
 285 winds related to low and high velocities observed in our data (Sec. 2.2).

286 3.2 Data distribution in the flow regimes

287 We can go one step further and analyse how our data quantitatively spread
 288 over the different regimes discussed above. For that purpose, one needs to
 289 compute kH and \mathcal{F} from the time series. H , U and the other atmospheric
 290 parameters can be deduced from the various vertical profiles (temperature,
 291 humidity) available in the ERA5 climate reanalysis (Online Resource section
 292 2). We quantify the flow deflection δ_θ as the minimal angle between the wind
 293 orientations comparing the local measurements and the regional predictions.
 294 We also compute the relative velocity modulation as

$$\delta_u = \frac{u_*^{\text{ERA5-Land}} - u_*^{\text{Local mes.}}}{u_*^{\text{ERA5-Land}}}. \quad (2)$$

295 These two quantities are represented as maps in the plane (\mathcal{F}, kH) (Fig. 8a,b),
 296 and one can clearly identify different regions in these graphs. Small wind dis-

turbances (small δ_θ and δ_u) are located in the top-right part of the diagrams, corresponding to a regime with low-interaction as well as low-confinement (kH and \mathcal{F} large enough, Fig. 7d). Lower values of kH (stronger interaction) or of Froude number (stronger confinement) both lead to an increase in wind disturbances, both in terms of orientation and velocity. Below a crossover value $kH \simeq 0.3$, wind disturbance is less sensitive to the \mathcal{F} -value. This is probably due to enhanced non-linear effects linked to flow modulation by the obstacle when confinement is strong (e.g. wakes and flow recirculations). The Froude number also controls a transition from damped to amplified wind velocities in the interdune, with a crossover around $\mathcal{F} \simeq 0.4$ (Fig. 8b). Such an amplification is rather unexpected. Checking the occurrence of the corresponding data, it appears that these amplifications are associated with the southerly sea breeze, and occur dominantly during the October-March period, when the other easterly wind is not present (Online Resource Fig. S12a–b). Furthermore, they occur less frequently during the afternoon, and more frequently at the end of the day (Online Resource Fig. S12c). This effect may be linked to a change in the flow behaviour in the lee side of the obstacles but further measurements are needed in order to assess the different possibilities (Baines 1995; Vosper 2004).

It is important to discuss the sensitivity of the results with respect to the choice of the hydrodynamic roughnesses (see Online Resource section 4). In fact, the only quantities dependent on this choice are those which involve the amplitude of the velocities: wind shear velocities, Froude number \mathcal{F} and relative velocity modulation δ_u . Those associated with wind direction are independent of this choice. Considering the possible range of realistic roughnesses values, the uncertainty on velocities estimated using the law of the wall is at most 30%. A similar maximum uncertainty applies to the Froude number. This uncertainty also propagates to δ_u , for which Figure S14 shows that the choice of roughness has little influence of its temporal variations, even if it can induce a global increase or decrease of its values. As such, the choice of z_0 will not qualitatively affect the overall aspect of the regime diagram presented in Figure 8b. It may only change the crossover value of δ_u at which the transition between regimes is observed (dashed green lines in that figure). Our conclusions are thus robust with respect to the somewhat arbitrary choice of the hydrodynamic roughnesses in the use of the data from ERA5-Land reanalysis.

332 4 Discussion and conclusion

The feedback of the giant dunes on the wind flow has important implications for smaller scales bedforms. As illustrated in Fig. 9, small linear dunes (~ 50 m wide) are often present in the 1–2 km interdune between giant linear dunes in the Namib Sand Sea (Livingstone et al. 2010). These smaller dunes do not exhibit the same orientation as the large ones, and are sometimes named ‘crossing dunes’ (Chandler et al. 2022). Whilst differences between large and small scale dune patterns are observed ubiquitously, they are usually attributed to

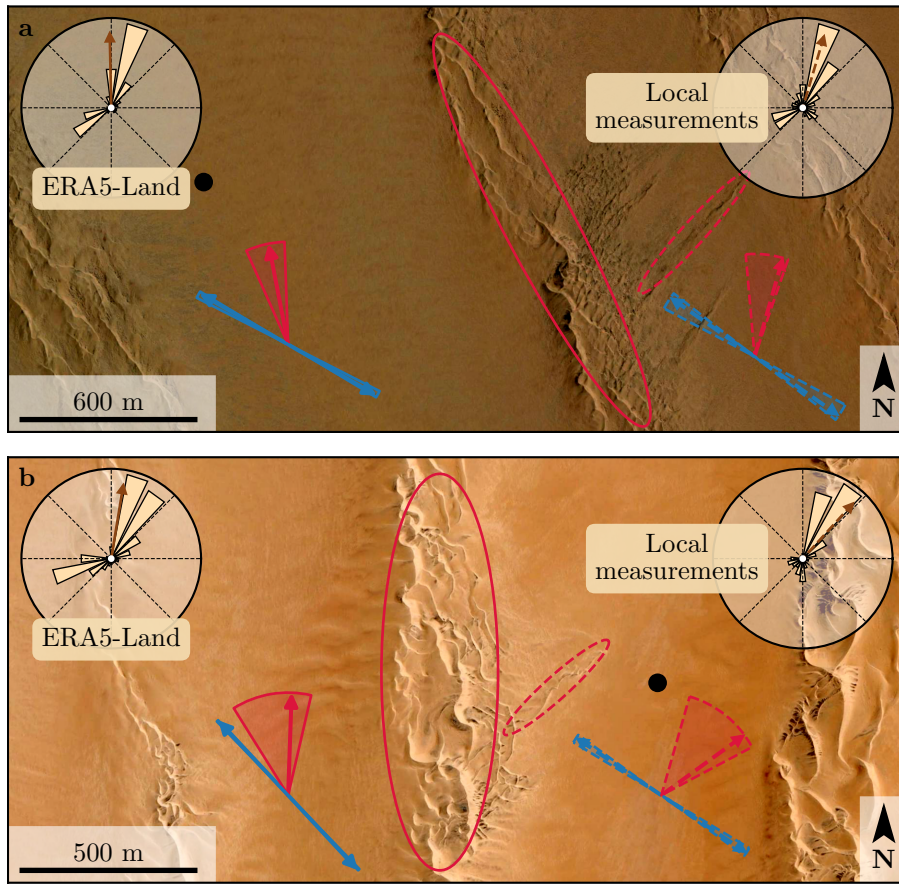


Fig. 9 Implications for smaller scale patterns in (a) the South Sand Sea and (b) North Sand Sea. The ellipses indicate the different types of elongating dunes, at large (plain line) and small (dashed line) scales. Dune orientation are predicted using the model of Courrech du Pont et al. (2014) from the sand flux angular distributions, shown here (roses) along with the resultant transport direction (brown arrow) for typical values (grain size $180 \mu\text{m}$, flux-up ratio of 1.6). Code for corresponding arrows: use of ERA5-Land data (plain line), use of local measurements (dashed line), prediction for the bed instability growth mechanism (blue), prediction for the elongation growth mechanism (red). Wedges show the uncertainty on the orientation calculation when parameters are varied. The black dots indicate the location of the meteorological stations in the interdune. See Appendix 2 for additional details.

340 the presence of two different dune growth mechanisms, leading to two dif-
 341 ferent dune patterns (orientations and/or morphologies) for the same wind
 342 regime (Courrech du Pont et al. 2014; Runyon et al. 2017; Lü et al. 2017; Song
 343 et al. 2019; Gadal et al. 2020; Hu et al. 2021). Here, however, our arguments
 344 enable the development of differing orientations for the small and giant lin-
 345 ear dunes governed by the same dune growth mechanism (elongating mode).
 346 Figure 9 shows how the orientations for the small and giant dunes can be
 347 derived from the locally measured and regionally predicted winds respectively

(red arrows in Fig. 9). These predictions require to specify the threshold of aeolian sand transport. Importantly, its value (a shear velocity estimated at $u_{th} \simeq 0.15 \text{ m s}^{-1}$) can be reached in periods during which winds are deflected (recall that the stronger winds, responsible for most of the sediment transport and associated dune morphodynamics, are not deflected – see Fig. 6). The feedback of the giant dunes on the wind described in this study, through wind deflection and attenuation, thus provides a potential explanation for the existence of these small linear dunes elongating across the interdune, a dynamic which has remained unresolved to date. These crossing dunes could provide additional constraints for the inference of local winds from bedforms, similarly to that currently performed on Mars using ripple orientations (Liu and Zimbelman 2015; Hood et al. 2021). Further work is needed to investigate these processes in more detail, including measurements of sediment transport and flow on the top of dunes.

This study presents the evidence that wind flow patterns around giant dunes are influenced by the atmospheric boundary layer, particularly during nocturnal conditions. However, we do not address here the question of the limitation of their pattern coarsening, and leave open the debate as to whether the size of giant dunes is controlled by the depth of this layer (Andreotti et al. 2009), in contrast to sediment supply limited and ever-slower growth with size (Werner and Kocurek 1999; Gunn et al. 2021a). More field evidence is definitively needed from additional dune fields, but this mechanism would allow for the inference of the ABL depth from giant bedform wavelengths where measurements are not feasible or available, such as Titan (Lorenz et al. 2010).

To conclude on conditions under which the ERA5-Land reanalysis data can reliably be used to study dune morphodynamics, we summarise the comparison of local (direct measurements) and regional (climate reanalysis) wind data as follows. In flat areas, the agreement between the two confirms the ability of the ERA5-Land climate reanalysis to predict the wind regime down to scales $\sim 10 \text{ km}$, i.e. the model grid. When smaller scale topographies are present (giant dunes in our case), locally measured winds can significantly differ from the regionally predicted ones. This is the case when the disturbances induced by the dunes interact with the lower part of the ABL vertical structure, which presents circadian variations. During the day, when the capping layer is typically high, this interaction is small, and the ERA5-Land predictions are also quantitatively consistent with the local data. During the night, however, the presence of a shallow atmospheric boundary layer induces a strong confinement of the flow, and is associated with large wind deflection by the dunes. Importantly, we find that this effect can be counterbalanced for large wind velocities, which are capable of deforming the capping layer, thus decreasing the influence of the confinement.

The theoretical computation of the wind disturbances induced by sinusoidal ridges under flow confinement has been performed in the linear limit (Andreotti et al. 2009, 2012), i.e. when the aspect ratio of these ridges is small ($k\xi_0 \ll 1$). These models are able to qualitatively reproduce the observed

wind deflection (Appendix 1, Online Resource Figs. S11 and S13), and thus provide the physical support for the interpretation we propose here based on hydrodynamic regimes. However, these models cannot quantitatively predict the magnitude of our observations, probably due to the presence of expected non-linearities in high confinement situations linked to strong flow modulations. Besides, these linear calculations only predict wind attenuation in the interdune, in contrast with the observed enhanced velocities associated with particular evening winds from the South during the period October-March (Online Resource Fig. S12). Some other models predict different spatial flow structures in response to a modulated topography, such as lee waves and rotors (Baines 1995; Vosper 2004). However, our measurements are located at a single point in the interdune, and we are thus unable to explore these types of responses. Data at different places along and across the ridges are needed to investigate and possibly map such flow structures, and for further comparisons with the models.

Acknowledgements We would like to acknowledge the contributors of the following open-source python librairies, Matplotlib (Hunter 2007), Numpy (Harris et al. 2020) and Scipy (Virtanen et al. 2020), which provide an incredibly efficient ecosystem allowing scientific research in Python. We also thank B. Andreotti and A. Gunn for useful discussions.

All data used in this study can be found in Gadal et al. (2022). Note that it contains modified Copernicus Climate Change Service Information (2021). Neither the European Commission nor ECMWF is responsible for any use that may be made of the Copernicus Information or Data it contains. Documented codes used in this study to analyse this data are available at <https://github.com/Cgadal/GiantDunes> (will be made public upon acceptance of this manuscript for publication).

Multiple grants have supported the collection of wind data through visits to the four sites between 2013 and 2020 (John Fell Oxford University Press (OUP) Research Fund (121/474); National Geographic (CP-029R-17); Natural Environment Research Council UK (NE/R010196/1 and NE/H021841/1 NSFGEO-NERC); Southampton Marine and Maritime Institute SMMI EPSRC-GCRF UK), along with research permits (1978/2014, 2140/2016, 2304/2017, 2308/2017, RPIV00022018, RPIV0052018, RPIV00230218). The authors are very grateful for support from Etosha National Park (especially Shyane Kötting, Boas Erckie, Pierre du Preez, Claudine Cloete, Immanuel Kapofi, Wilferd Versfeld, and Werner Kilian), Gobabeb Namib Research Institute (Gillian Maggs-Kölling and Eugene Marais), The Skeleton Coast National Park (Joshua Kazzeurua). Various researchers and desert enthusiasts have assisted with instruments and the logistics of expeditions, especially Mary Seely for expert guidance at the North Sand Sea site.

Finally, we acknowledge financial support from the Laboratoire d'Excellence UnivEarthS Grant ANR-10-LABX-0023, the Initiative d'Excellence Université de Paris Grant ANR-18-IDEX-0001, the French National Research Agency Grants ANR-17-CE01-0014/SONO and the National Science Center of Poland Grant 2016/23/B/ST10/01700.

Appendix 1: Linear theory of wind response to topographic perturbation

Following the work of Fourrière et al. (2010), Andreotti et al. (2012) and Andreotti et al. (2009), we briefly describe in this appendix the framework for the linear response of a turbulent flow to a topographic perturbation of small aspect ratio. As a general bed elevation can be decomposed into Fourier

⁴⁴¹ modes, we focus here on a sinusoidal topography:

$$\xi = \xi_0 \cos [k (\cos(\alpha)y - \sin(\alpha)x)], \quad (3)$$

⁴⁴² which is also a good approximation for the giant dunes observed in the North
⁴⁴³ Sand Sea and South Sand Sea Station (Fig. 2 and Online Resource Fig. S4).
⁴⁴⁴ Here, x and y are the streamwise and spanwise coordinates, $k = 2\pi/\lambda$ the
⁴⁴⁵ wavenumber of the sinusoidal perturbation, α its crest orientation with respect
⁴⁴⁶ to the x -direction (anticlockwise) and ξ_0 its amplitude. The two components
⁴⁴⁷ of the basal shear stress $\tau = \rho_0 u_* \mathbf{u}_*$, constant in the flat bottom reference
⁴⁴⁸ case, can then be generically written as:

$$\tau_x = \tau_0 \left(1 + k\xi_0 \sqrt{\mathcal{A}_x^2 + \mathcal{B}_x^2} \cos [k (\cos(\alpha)y - \sin(\alpha)x) + \phi_x] \right), \quad (4)$$

$$\tau_y = \tau_0 k\xi_0 \sqrt{\mathcal{A}_y^2 + \mathcal{B}_y^2} \cos [k (\cos(\alpha)y - \sin(\alpha)x) + \phi_y], \quad (5)$$

⁴⁴⁹ where τ_0 is the reference basal shear stress on a flat bed. We have defined
⁴⁵⁰ the phase $\phi_{x,y} = \tan^{-1}(\mathcal{B}_{x,y}/\mathcal{A}_{x,y})$ from the in-phase and in-quadrature hydrodynamical
⁴⁵¹ coefficients $\mathcal{A}_{x,y}$ and $\mathcal{B}_{x,y}$. They are functions of k and of the
⁴⁵² flow conditions, i.e the bottom roughness, the vertical flow structure and the
⁴⁵³ incident flow direction, and the theoretical framework developed in the above
⁴⁵⁴ cited papers proposes methods to compute them in the linear regime.

⁴⁵⁵ Following Andreotti et al. (2012), the effect of the incident wind direction
⁴⁵⁶ can be approximated by the following expressions:

$$\mathcal{A}_x = \mathcal{A}_0 \sin^2 \alpha, \quad (6)$$

$$\mathcal{B}_x = \mathcal{B}_0 \sin^2 \alpha, \quad (7)$$

$$\mathcal{A}_y = -\frac{1}{2} \mathcal{A}_0 \cos \alpha \sin \alpha, \quad (8)$$

$$\mathcal{B}_y = -\frac{1}{2} \mathcal{B}_0 \cos \alpha \sin \alpha, \quad (9)$$

⁴⁵⁷ where \mathcal{A}_0 and \mathcal{B}_0 are now two coefficients independent of the dune orientation
⁴⁵⁸ α , corresponding to the transverse case ($\alpha = 90^\circ$). In the case of a fully
⁴⁵⁹ turbulent boundary layer capped by a stratified atmosphere, these coefficients
⁴⁶⁰ depend on kH , kz_0 , \mathcal{F} and \mathcal{F}_1 (Andreotti et al. 2009). For their computation,
⁴⁶¹ we assume here a constant hydrodynamic roughness $z_0 \simeq 1$ mm (Online Re-
⁴⁶² source section 1). For the considered giant dunes, this leads to $kz_0 \simeq 2 \cdot 10^{-6}$,
⁴⁶³ as their wavelength is $\lambda \simeq 2.4$ km (or $k \simeq 2 \cdot 10^{-3} \text{ m}^{-1}$). Values of z_0 extracted
⁴⁶⁴ from field data indeed typically fall between 0.1 mm and 10 mm (Sherman and
⁴⁶⁵ Farrell 2008; Field and Pelletier 2018). Importantly, \mathcal{A}_0 and \mathcal{B}_0 do not vary
⁴⁶⁶ much in the corresponding range of kz_0 (Fourrière et al. 2010), and the results
⁴⁶⁷ presented here are robust with respect to this choice.

⁴⁶⁸ With capping layer height and Froude numbers computed from the ERA5-
⁴⁶⁹ Land time series, the corresponding \mathcal{A}_0 and \mathcal{B}_0 can be deduced, as displayed
⁴⁷⁰ in Online Resource Fig. S13. Interestingly, it shows similar regimes as in the
⁴⁷¹ diagrams of Fig. 8 and Online Resource Fig. S11a,b, supporting the underly-
⁴⁷² ing physics. However, the agreement is qualitative only. Further, the linearity

assumption of the theoretical framework requires $(|\tau| - \tau_0)/\tau_0 \ll 1$, which translates into $k\xi\sqrt{\mathcal{A}_0^2 + \mathcal{B}_0^2} \ll 1$. In our case, the giant dune morphology gives $k\xi_0 \simeq 0.1$, which means that one quits the regime of validity of the linear theory when the coefficient modulus $\sqrt{\mathcal{A}_0^2 + \mathcal{B}_0^2}$ becomes larger than a few units. In accordance with the theoretical expectations, these coefficients present values on the order of unity ($\mathcal{A}_0 \simeq 3$ and $\mathcal{B}_0 \simeq 1$) in unconfined situations (Claudin et al. 2013; Lü et al. 2021). In contrast and as illustrated in Online Resource Fig. S13a,b, larger values are predicted in case of strong confinement, which does not allow us to proceed to further quantitative comparison with the data.

Finally, the linear model is also able to reproduce the enhancement of the flow deflection over the sinusoidal ridges when $\sqrt{\mathcal{A}_0^2 + \mathcal{B}_0^2}$ is increased (Online Resource Fig. S13). Here, using $k\xi_0 \simeq 0.1$ to be representative of the amplitude of the giant dunes at the North Sand Sea station, the coefficient modulus is bounded to 10.

Appendix 2: Sediment transport and dune morphodynamics

We summarise in this appendix the sediment transport and dune morphodynamics theoretical framework leading to the prediction of sand fluxes and dune orientations from wind data.

Sediment transport — The prediction of sand fluxes from wind data has been a long standing issue in aeolian geomorphological studies (Fryberger and Dean 1979; Pearce and Walker 2005; Sherman and Li 2012; Shen et al. 2019). Based on laboratory studies in wind tunnels (Rasmussen et al. 1996; Iversen and Rasmussen 1999; Creyssels et al. 2009; Ho et al. 2011), as well as physical considerations (Ungar and Haff 1987; Andreotti 2004; Durán et al. 2011; Páhtz and Durán 2020), it has been shown that the steady saturated saltation flux over a flat sand bed depends linearly on the shear stress:

$$\frac{q_{\text{sat}}}{Q} = \Omega \sqrt{\Theta_{\text{th}}} (\Theta - \Theta_{\text{th}}), \quad (10)$$

where Ω is a proportionality constant, $Q = d\sqrt{(\rho_s - \rho_0)gd/\rho_0}$ is a characteristic flux, $\Theta = \rho_0 u_*^2 / (\rho_s - \rho_0)gd$ the Shields number, and Θ_{th} its threshold value below which saltation vanishes. $\rho_s = 2.6 \text{ g cm}^{-3}$ and $d = 180 \mu\text{m}$ are the grain density and diameter, and g is the gravitational acceleration. The shear velocity, and consequently the Shields number as well as the sediment flux, are time dependent.

Recently, Páhtz and Durán (2020) suggested an additional quadratic term in Shields to account for grain-grain interactions within the transport layer at strong wind velocities:

$$\frac{q_{\text{sat}, t}}{Q} = \frac{2\sqrt{\Theta_{\text{th}}}}{\kappa\mu} (\Theta - \Theta_{\text{th}}) \left(1 + \frac{C_M}{\mu} [\Theta - \Theta_{\text{th}}] \right), \quad (11)$$

509 where $\kappa = 0.4$ is the von Kármán constant, $C_M \simeq 1.7$ a constant and $\mu \simeq 0.6$ is
 510 a friction coefficient, taken to be the avalanche slope of the granular material.
 511 The fit of this law to the experimental data of Creyssels et al. (2009) and Ho
 512 et al. (2011) gives $\Theta_{\text{th}} = 0.0035$. The fit of Eq. 10 on these same data similarly
 513 gives $\Omega \simeq 8$ and $\Theta_{\text{th}} = 0.005$. The sand flux angular distributions and the
 514 dune orientations in Fig. 9 are calculated using this law (11). We have checked
 515 that using the ordinary linear relationship (10) instead does not change the
 516 predicted dune orientations by more than a few degrees.

517 *Dune orientations* — Dune orientations are predicted with the dimensional
 518 model of Courrech du Pont et al. (2014), from the sand flux time series com-
 519 puted with the above transport law. Two orientations are possible depending
 520 on the mechanism dominating the dune growth: elongation or bed instabil-
 521 ity. The orientation α corresponding the bed instability is then the one that
 522 maximises the following growth rate (Rubin and Hunter 1987):

$$\sigma \propto \frac{1}{H_d W_d T} \int_0^T q_{\text{crest}} |\sin(\theta - \alpha)| dt, \quad (12)$$

523 where θ is the wind orientation measured with respect to the same reference
 524 as α , and H_d and W_d are dimensional constants respectively representing the
 525 dune height and width. The integral runs over a time T , which must be repre-
 526 sentative of the characteristic period of the wind regime. The flux at the crest
 527 is expressed as:

$$q_{\text{crest}} = q_{\text{sat}} [1 + \gamma |\sin(\theta - \alpha)|], \quad (13)$$

528 where the flux-up ratio γ has been calibrated to 1.6 using field studies, under-
 529 water laboratory experiments and numerical simulations. Predictions of the
 530 linear analysis of Gadal et al. (2019) and Delorme et al. (2020) give similar
 531 results.

532 Similarly, the dune orientation corresponding to the elongation mechanism
 533 is the one that verifies:

$$\tan(\alpha) = \frac{\langle q_{\text{crest}}(\alpha) e_\theta \rangle \cdot e_{WE}}{\langle q_{\text{crest}}(\alpha) e_\theta \rangle \cdot e_{SN}}, \quad (14)$$

534 where $\langle \cdot \rangle$ denotes a vectorial time average. The unitary vectors e_{WE} , e_{SN} and
 535 e_θ are in the West-East, South-North and wind directions, respectively.

536 The resulting computed dune orientations, blue and red arrows in Fig. 9,
 537 then depend on a certain number of parameters (grain properties, flux-up ratio,
 538 etc.), for which we take typical values for aeolian sandy deserts. Due to the lack
 539 of measurements in the studied places, some uncertainties can be expected. We
 540 therefore run a sensitivity test by calculating the dune orientations for grain
 541 diameters ranging from $100 \mu\text{m}$ to $400 \mu\text{m}$ and for a speed-up ratio between
 542 0.1 and 10 (wedges in Fig. 9).

543 References

- 544 Andreotti B (2004) A two-species model of aeolian sand transport. *J Fluid
545 Mech* 510:47–70
- 546 Andreotti B, Claudin P, Douady S (2002) Selection of dune shapes and veloc-
547 ities part 1: Dynamics of sand, wind and barchans. *The European Physical
548 Journal B-Condensed Matter and Complex Systems* 28:321–339
- 549 Andreotti B, Fourrière A, Ould-Kaddour F, Murray B, Claudin P (2009) Gi-
550 ant aeolian dune size determined by the average depth of the atmospheric
551 boundary layer. *Nature* 457:1120–1123
- 552 Andreotti B, Claudin P, Devauchelle O, Durán O, Fourrière A (2012) Bedforms
553 in a turbulent stream: ripples, chevrons and antidunes. *J Fluid Mech* 690:94–
554 128
- 555 Ashkenazy Y, Yizhaq H, Tsoar H (2012) Sand dune mobility under climate
556 change in the kalahari and australian deserts. *Climatic Change* 112:901–923
- 557 Baddock M, Livingstone I, Wiggs G (2007) The geomorphological significance
558 of airflow patterns in transverse dune interdunes. *Geomorphology* 87:322–
559 336
- 560 Bagnold RA (1941) *The Physics of Blown Sand and Desert Dunes*. London :
561 Methuen : Chapman & Hall
- 562 Baines PG (1995) Topographic effects in stratified flows. Cambridge university
563 press
- 564 Bauer BO, Sherman DJ, Wolcott JF (1992) Sources of uncertainty in shear
565 stress and roughness length estimates derived from velocity profiles. *The
566 Professional Geographer* 44:453–464
- 567 Belcher S, JCR H (1998) Turbulent flow over hills and waves. *Annu Rev Fluid
568 Mech* 30:507–538
- 569 Blumberg DG, Greeley R (1996) A comparison of general circulation model
570 predictions to sand drift and dune orientations. *J Clim* 9:3248–3259
- 571 Bristow NR, Best J, Wiggs GFS, Nield JM, Baddock MC, Delorme P, Chris-
572 tensen KT (2022) Topographic perturbation of turbulent boundary layers
573 by low-angle, early-stage aeolian dunes. *Earth Surf Process Landf* n/a, DOI
574 <https://doi.org/10.1002/esp.5326>
- 575 Brookfield M (1977) The origin of bounding surfaces in ancient aeolian sand-
576 stones. *Sedimentology* 24:303–332
- 577 Brown S, Nickling WG, Gillies JA (2008) A wind tunnel examination of shear
578 stress partitioning for an assortment of surface roughness distributions. *J
579 Geophys Res* 113:F02S06
- 580 Chandler C, Radebaugh J, McBride J, Morris T, Narteau C, Arnold K, Lorenz
581 R, Barnes J, Hayes A, Rodriguez S, Rittenour T (2022) Near-surface struc-
582 ture of a large linear dune and an associated crossing dune of the northern
583 namib sand sea from ground penetrating radar: Implications for the his-
584 tory of large linear dunes on earth and titan. *Aeolian Research* 57:100813,
585 DOI <https://doi.org/10.1016/j.aeolia.2022.100813>
- 586 Chang H, Simons D (1970) The bed configuration of straight sand-bed channels
587 when flow is nearly critical. *J Fluid Mech* 42:491–495

- 588 Charru F, Andreotti B, Claudin P (2013) Sand ripples and dunes. *Annu Rev Fluid Mech* 45:469–493
- 589
- 590 Claudin P, Wiggs G, Andreotti B (2013) Field evidence for the upwind velocity shift at the crest of low dunes. *Boundary-Layer Meteorol* 148:195–206
- 591
- 592 Claudin P, Durán O, Andreotti B (2017) Dissolution instability and roughening transition. *J Fluid Mech* 832:R2
- 593
- 594 Claudin P, Louge M, Andreotti B (2021) Basal pressure variations induced by a turbulent flow over a wavy surface. *Frontiers in Physics* 9:682564
- 595
- 596 Colombini M (2004) Revisiting the linear theory of sand dune formation. *J Fluid Mech* 502:1–16
- 597
- 598 Courrech du Pont S (2015) Dune morphodynamics. *C R Phys* 16:118–138
- 599 Courrech du Pont S, Narteau C, Gao X (2014) Two modes for dune orientation. *Geology* 42:743–746
- 600
- 601 Creyssels M, Dupont P, El Mohtar AO, Valance A, Cantat I, Jenkins JT, Pasini JM, Rasmussen KR (2009) Saltating particles in a turbulent boundary layer: experiment and theory. *J Fluid Mech* 625:47–74
- 602
- 603 de Winter W, Donker J, Sterk G, Van Beem J, Ruessink G (2020) Regional versus local wind speed and direction at a narrow beach with a high and steep foredune. *Plos one* 15:e0226983
- 604
- 605 Dee DP, Uppala SM, Simmons AJ, Berrisford P, Poli P, Kobayashi S, Andrae U, Balmaseda M, Balsamo G, Bauer dP, et al. (2011) The era-interim re-analysis: Configuration and performance of the data assimilation system. *Q J R Meteorol Soc* 137:553–597
- 606
- 607 Delorme P, Wiggs G, Baddock M, Claudin P, Nield J, Valdez A (2020) Dune initiation in a bimodal wind regime. *J Geophys Res* 125:e2020JF005757
- 608
- 609 Durán O, Claudin P, Andreotti B (2011) On aeolian transport: Grain-scale interactions, dynamical mechanisms and scaling laws. *Aeolian Res* 3:243–270
- 610
- 611 Durran DR (1990) Mountain waves and downslope winds. In: *Atmospheric processes over complex terrain*, Springer, pp 59–81
- 612
- 613 Dyer A (1974) A review of flux-profile relationships. *Boundary-Layer Meteorol* 7:363–372
- 614
- 615 Ewing RC, Kocurek G, Lake LW (2006) Pattern analysis of dune-field parameters. *Earth Surf Process Landf* 31:1176–1191
- 616
- 617 Farr TG, Rosen PA, Caro E, Crippen R, Duren R, Hensley S, Kobrick M, Paller M, Rodriguez E, Roth L, et al. (2007) The shuttle radar topography mission. *Rev Geophys* 45
- 618
- 619 Fernando H, Mann J, Palma J, Lundquist JK, Barthelmie RJ, Belo-Pereira M, Brown W, Chow F, Gerz T, Hocut C, et al. (2019) The perdigão: Peering into microscale details of mountain winds. *Bull Am Meteorol Soc* 100:799–819
- 620
- 621 Field JP, Pelletier JD (2018) Controls on the aerodynamic roughness length and the grain-size dependence of aeolian sediment transport. *Earth Surf Process Landf* 43:2616–2626
- 622
- 623 Finnigan J, Raupach M, Bradley E, Aldis G (1990) A wind tunnel study of turbulent flow over a two-dimensional ridge. *Boundary-Layer Meteorol*
- 624
- 625
- 626
- 627
- 628
- 629
- 630
- 631
- 632
- 633

- 634 50:277–317
- 635 Finnigan J, Ayotte K, Harman I, Katul G, Oldroyd H, Patton E, Poggi D,
636 Ross A, Taylor P (2020) Boundary-layer flow over complex topography.
Boundary-Layer Meteorol 177:247–313
- 638 Flack K, Schultz M (2010) Review of hydraulic roughness scales in the fully
639 rough regime. Journal of Fluids Engineering 132:041203
- 640 Fourrière A, Claudin P, Andreotti B (2010) Bedforms in a turbulent stream:
641 formation of ripples by primary linear instability and of dunes by nonlinear
642 pattern coarsening. J Fluid Mech 649:287–328
- 643 Frederick KA, Hanratty TJ (1988) Velocity measurements for a turbulent non-
644 separated flow over solid waves. Exp Fluids 6:477–486
- 645 Fryberger SG, Dean G (1979) Dune forms and wind regime. A study of global
646 sand seas 1052:137–169
- 647 Gadal C, Narteau C, Courrech Du Pont S, Rozier O, Claudin P (2019) Incip-
648 ient bedforms in a bidirectional wind regime. J Fluid Mech 862:490–516
- 649 Gadal C, Narteau C, Courrech du Pont S, Rozier O, Claudin P (2020) Peri-
650 odicity in fields of elongating dunes. Geology 48:343–347
- 651 Gadal C, Delorme P, Narteau C, Wiggs G, Baddock M, Nield JM, Claudin
652 P (2022) Data used in 'Local wind regime induced by giant linear dunes:
653 comparison of ERA5-Land re-analysis with surface measurements'. DOI
654 10.5281/zenodo.6343138
- 655 Garratt JR (1994) The atmospheric boundary layer. Earth-Science Reviews
656 37:89–134
- 657 Garvey B, Castro IP, Wiggs G, Bullard J (2005) Measurements of flows over
658 isolated valleys. Boundary-Layer Meteorol 117:417–446
- 659 Gong W, Ibbetson A (1989) A wind tunnel study of turbulent flow over model
660 hills. Boundary-Layer Meteorol 49:113–148
- 661 Gong W, Taylor P, Dörnbrack A (1996) Turbulent boundary-layer flow over
662 fixed aerodynamically rough two-dimensional sinusoidal waves. J Fluid Mech
663 312:1–37
- 664 Guérin A, Derr J, Du Pont SC, Berhanu M (2020) Streamwise dissolution
665 patterns created by a flowing water film. Phys Rev Lett 125:194502
- 666 Gunn A, Casasanta G, Di Liberto L, Falcini F, Lancaster N,
667 Jerolmack DJ (2021a) What sets aeolian dune height? DOI
668 <https://doi.org/10.31223/X5QG8S>
- 669 Gunn A, Wanker M, Lancaster N, Edmonds D, Ewing R, Jerolmack
670 D (2021b) Circadian rhythm of dune-field activity. Geophys Res Lett
671 48:e2020GL090924
- 672 Harris CR, Millman KJ, van der Walt SJ, Gommers R, Virtanen P, Cournau-
673 peau D, Wieser E, Taylor J, Berg S, Smith NJ, et al. (2020) Array program-
674 ming with numpy. Nature 585:357–362
- 675 Havholm KG, Kocurek G (1988) A preliminary study of the dynamics of a
676 modern draa, algodones, southeastern california, usa. Sedimentology 35:649–
677 669
- 678 Hersbach H, Bell B, Berrisford P, Hirahara S, Horányi A, Muñoz-Sabater J,
679 Nicolas J, Peubey C, Radu R, Schepers D, et al. (2020) The era5 global

- 680 reanalysis. *Q J R Meteorol Soc* 146:1999–2049
- 681 Hesp P, Illenberger W, Rust I, McLachlan A, Hyde R (1989) Some aspects of
682 transgressive dunefield and transverse dune geomorphology and dynamics,
683 south coast, south africa. *Zeitschrift fur Geomorphologie*, Supplementband
684 73:111–123
- 685 Hesp PA, Hastings K (1998) Width, height and slope relationships and aero-
686 dynamic maintenance of barchans. *Geomorphology* 22:193–204
- 687 Hesp PA, Smyth TAG, Nielsen P, Walker IJ, Bauer BO, Davidson-Arnott R
688 (2015) Flow deflection over a foredune. *Geomorphology* 230:64–74
- 689 Ho TD, Valance A, Dupont P, Ould El Moctar A, Tuan Duc H, Valance A,
690 Dupont P, Ould El Moctar A (2011) Scaling laws in aeolian sand transport.
691 *Phys Rev Lett* 106:4–7
- 692 Hood DR, Ewing RC, Roback KP, Runyon K, Avouac JP, McEnroe M (2021)
693 Inferring airflow across martian dunes from ripple patterns and dynamics.
694 *Frontiers in Earth Science* 9:702828
- 695 Howard AD (1977) Effect of slope on the threshold of motion and its applica-
696 tion to orientation of wind ripples. *Geological Society of America Bulletin*
697 88:853–856
- 698 Hu Z, Gao X, Lei J, Zhou N (2021) Geomorphology of aeolian dunes in the
699 western sahara desert. *Geomorphology* 392:107916
- 700 Hunt J, Leibovich S, Richards K (1988) Turbulent shear flows over low hills.
701 *Q J R Meteorol Soc* 114:1435–1470
- 702 Hunt JCR, Vilenski GG, Johnson ER (2006) Stratified separated flow around
703 a mountain with an inversion layer below the mountain top. *J Fluid Mech*
704 556:105–119
- 705 Hunter JD (2007) Matplotlib: A 2d graphics environment. *Computing in sci-
706 ence & engineering* 9:90–95
- 707 Hunter RE, Richmond BM, Alpha TR (1983) Storm-controlled oblique dunes
708 of the oregon coast. *Geol Soc America Bull* 94:1450–1465
- 709 Iversen JD, Rasmussen KR (1999) The effect of wind speed and bed slope on
710 sand transport. *Sedimentology* 46:723–731
- 711 Jackson PS, Hunt JCR (1975) Turbulent wind flow over a low hill. *Q J R
712 Meteorol Soc* 101:929–955
- 713 Jiang Q (2014) Applicability of reduced-gravity shallow-water theory to atmo-
714 spheric flow over topography. *J Atmos Sci* 71:1460–1479
- 715 Jolivet M, Braucher R, Dovchintseren D, Hocquet S, Schmitt J, ASTER Team
716 (2021) Erosion around a large-scale topographic high in a semi-arid sedimen-
717 tary basin: Interactions between fluvial erosion, aeolian erosion and aeolian
718 transport. *Geomorphology* 386:107747
- 719 Kennedy JF (1963) The mechanics of dunes and antidunes in erodible-bed
720 channels. *J Fluid Mech* 16:521–544
- 721 Kim HG, Patel VC, Lee CM (2000) Numerical simulation of wind flow over
722 hilly terrain. *J Wind Eng Ind Aerodyn* 87:45–60
- 723 Kroy K, Sauermann G, Herrmann HJ (2002) Minimal model for aeolian sand
724 dunes. *Phys Rev E* 66:031302

- 725 Lancaster J, Lancaster N, Seely M (1984) Climate of the central namib desert.
726 Madoqua 1984:5–61
- 727 Lancaster N (1985) Winds and sand movements in the namib sand sea. Earth
728 Surf Process Landf 10:607–619
- 729 Lancaster N, Nickling W, Neuman CM, Wyatt V (1996) Sediment flux and
730 airflow on the stoss slope of a barchan dune. Geomorphology 17:55–62
- 731 Lewis HW, Mobbs SD, Lehning M (2008) Observations of cross-ridge flows
732 across steep terrain. Q J R Meteorol Soc 134:801–816
- 733 Liu ZYC, Zimbelman JR (2015) Recent near-surface wind directions inferred
734 from mapping sand ripples on martian dunes. Icarus 261:169–181
- 735 Livingstone I, Warren A (2019) Aeolian geomorphology: a new introduction.
736 Wiley
- 737 Livingstone I, Bristow C, Bryant RG, Bullard J, White K, Wiggs GFS, Baas
738 ACW, Bateman MD, Thomas DSG (2010) The namib sand sea digital
739 database of aeolian dunes and key forcing variables. Aeolian Res 2:93–104
- 740 Lorenz R, Claudin P, Andreotti B, Radebaugh J, Tokano T (2010) A 3 km
741 atmospheric boundary layer on titan indicated by dune spacing and huygens
742 data. Icarus 205:719–721
- 743 Lü P, Narteau C, Dong Z, Rozier O, Du Pont SC (2017) Unravelling raked
744 linear dunes to explain the coexistence of bedforms in complex dunefields.
745 Nature communications 8:1–9
- 746 Lü P, Narteau C, Dong Z, Claudin P, Rodriguez S, An Z, Fernandez-Cascales
747 L, Gadale C, Courrech du Pont S (2021) Direct validation of dune instability
748 theory. Proceedings of the National Academy of Sciences 118
- 749 Mason P, Sykes R (1979) Flow over an isolated hill of moderate slope. Q J R
750 Meteorol Soc 105:383–395
- 751 McKenna Neuman C, Lancaster N, Nickling WG (1997) Relations between
752 dune morphology, air flow, and sediment flux on reversing dunes, Silver Peak,
753 Nevada. Sedimentology 44:1103–1111, DOI 10.1046/j.1365-3091.1997.d01-
754 61.x
- 755 Mizumura K (1995) Free-surface profile of open-channel flow with wavy bound-
756 ary. J Hydraul Eng 121:533–539
- 757 Monin AS, Obukhov AM (1954) Basic laws of turbulent mixing in the surface
758 layer of the atmosphere. Contrib Geophys Inst Acad Sci USSR 151:e187
- 759 Mulligan KR (1988) Velocity profiles measured on the windward slope of a
760 transverse dune. Earth Surf Process Landf 13:573–582
- 761 Muñoz-Sabater J, Dutra E, Agustí-Panareda A, Albergel C, Arduini G, Bal-
762 samo G, Boussetta S, Choulga M, Harrigan S, Hersbach H, et al. (2021)
763 Era5-land: A state-of-the-art global reanalysis dataset for land applications.
764 Earth Syst Sci Data 13:4349–4383
- 765 Nield JM, King J, Wiggs GFS, Leyland J, Bryant RG, Chiverrell RC, Darby
766 SE, Eckhardt FD, Thomas DSG, Vircavs LH, Washington R (2014) Esti-
767 mating aerodynamic roughness over complex surface terrain. J Geophys Res
768 118:12948–12961
- 769 Nield JM, Wiggs GF, Baddock MC, Hipondoka MH (2017) Coupling leeside
770 rainfall to avalanche characteristics in aeolian dune dynamics. Geology

- 771 45:271–274
- 772 Pähzt T, Durán O (2020) Unification of aeolian and fluvial sediment transport
773 rate from granular physics. *Phys Rev Lett* 124:168001
- 774 Pearce KI, Walker IJ (2005) Frequency and magnitude biases in the 'Fryberger'
775 model, with implications for characterizing geomorphically effective winds.
776 *Geomorphology* 68:39–55
- 777 Pelletier JD, Field JP (2016) Predicting the roughness length of turbulent flows
778 over landscapes with multi-scale microtopography. *Earth Surface Dynamics*
779 4:391–405
- 780 Poggi D, Katul G, Albertson J, Ridolfi L (2007) An experimental investigation
781 of turbulent flows over a hilly surface. *Phys Fluids* 19:036601
- 782 Rasmussen KR (1989) Some aspects of flow over coastal dunes. *Proceedings of*
783 *the Royal Society of Edinburgh, Section B: Biological Sciences* 96:129–147
- 784 Rasmussen KR, Iversen JD, Rautaheimo P (1996) Saltation and wind flow
785 interaction in a variable slope wind tunnel. *Geomorphology* 17:19–28
- 786 Raupach M (1992) Drag and drag partition on rough surfaces. *Boundary-Layer*
787 *Meteorol* 60:375–395
- 788 Rubin DM, Hunter RE (1987) Bedform alignment in directionally varying
789 flows. *Science* 237:276–278
- 790 Runyon K, Bridges N, Ayoub F, Newman C, Quade J (2017) An integrated
791 model for dune morphology and sand fluxes on mars. *Earth and Planetary*
792 *Science Letters* 457:204–212
- 793 Sauermann G, Andrade Jr J, Maia L, Costa U, Araújo A, Herrmann H
794 (2003) Wind velocity and sand transport on a barchan dune. *Geomorphology*
795 54:245–255
- 796 Seidel DJ, Zhang Y, Beljaars A, Golaz JC, Jacobson AR, Medeiros B (2012)
797 Climatology of the planetary boundary layer over the continental united
798 states and europe. *J Geophys Res* 117:D17106
- 799 Shao Y (2008) Physics and modelling of wind erosion, vol 37. Springer Science
800 & Business Media
- 801 Shen Y, Zhang C, Huang X, Wang X, Cen S (2019) The effect of wind speed
802 averaging time on sand transport estimates. *Catena* 175:286–293
- 803 Sheridan PF, Vosper SB (2006) A flow regime diagram for forecasting lee
804 waves, rotors and downslope winds. *Meteorol Appl* 13:179–195
- 805 Sherman CA (1978) A mass-consistent model for wind fields over complex
806 terrain. *J Appl Meteorol Clim* 17:312–319
- 807 Sherman D, Farrell E (2008) Aerodynamic roughness lengths over movable
808 beds: Comparison of wind tunnel and field data. *J Geophys Res* 113:1–10
- 809 Sherman DJ, Li B (2012) Predicting aeolian sand transport rates: A reevalu-
810 ation of models. *Aeolian Res* 3:371–378
- 811 Smith AB, Jackson DWT, Cooper JAG (2017) Three-dimensional airflow and
812 sediment transport patterns over barchan dunes. *Geomorphology* 278:28–42
- 813 Song Q, Gao X, Lei J, Li S (2019) Spatial distribution of sand dunes and their
814 relationship with fluvial systems on the southern margin of the taklimakan
815 desert, china. *Geomatics, Natural Hazards and Risk* 10:2408–2428

- 816 Spalding DB (1961) A single formula for the law of the wall. *Journal of Applied*
817 *Mechanics* 28:455–458
- 818 Stull R (2006) 9 - the atmospheric boundary layer. In: Wallace JM, Hobbs PV
819 (eds) *Atmospheric Science* (Second Edition), second edition edn, Academic
820 Press, San Diego, pp 375–417
- 821 Stull RB (1988) An introduction to boundary layer meteorology, vol 13.
822 Springer Science & Business Media
- 823 Sullivan PP, McWilliams JC (2010) Dynamics of winds and currents coupled
824 to surface waves. *Annu Rev Fluid Mech* 42:19–42
- 825 Sweet M, Kocurek G (1990) An empirical model of aeolian dune lee-face air-
826 flow. *Sedimentology* 37:1023–1038
- 827 Sykes RI (1980) An asymptotic theory of incompressible turbulent boundary-
828 layer flow over a small hump. *J Fluid Mech* 101:647–670
- 829 Taylor P, Teunissen H (1987) The Askervein hill project: overview and back-
830 ground data. *Boundary-Layer Meteorol* 39:15–39
- 831 Taylor P, Mason P, Bradley E (1987) Boundary-layer flow over low hills.
832 *Boundary-Layer Meteorol* 39:107–132
- 833 Tsoar H, Yaalon DH (1983) Deflection of sand movement on a sinuous longi-
834 tudinal (seif) dune: use of fluorescent dye as tracer. *Sedimentary Geology*
835 36:25–39
- 836 Ungar JE, Haff PK (1987) Steady state saltation in air. *Sedimentology* 34:289–
837 299
- 838 Unsworth C, Parsons D, Hardy R, Reesink A, Best J, Ashworth P, Keevil G
839 (2018) The impact of nonequilibrium flow on the structure of turbulence
840 over river dunes. *Water Resour Res* 54:6566–6584
- 841 Uppala SM, Källberg P, Simmons AJ, Andrae U, Bechtold VDC, Fiorino M,
842 Gibson J, Haseler J, Hernandez A, Kelly G, et al. (2005) The era-40 re-
843 analysis. *Q J R Meteorol Soc* 131:2961–3012
- 844 Valance A, Rasmussen K, Ould El Moctar A, Dupont P (2015) The physics
845 of aeolian sand transport. *C R Phys* 16:1–13
- 846 Venditti JG, Best JL, Church M, Hardy RJ (2013) Coherent Flow Structures
847 at Earth's Surface. John Wiley & Sons
- 848 Virtanen P, Gommers R, Oliphant TE, Haberland M, Reddy T, Cournapeau
849 D, Burovski E, Peterson P, Weckesser W, Bright J, et al. (2020) Scipy 1.0:
850 fundamental algorithms for scientific computing in python. *Nature methods*
851 17:261–272
- 852 Vogelegang D, Holtslag A (1996) Evaluation and model impacts of alternative
853 boundary-layer height formulations. *Boundary-Layer Meteorol* 81:245–269
- 854 Vosper SB (2004) Inversion effects on mountain lee waves. *Q J R Meteorol Soc*
855 130:1723–1748
- 856 Walker I, Davidson-Arnott R, Bauer B, Hesp P, Delgado-Fernandez I, Oller-
857 head J, Smyth T (2017) Scale-dependent perspectives on the geomorphology
858 and evolution of beach-dune systems. *Earth-Science Review* 171:220–253
- 859 Walker IJ, Nickling WG (2002) Dynamics of secondary airflow and sediment
860 transport over and in the lee of transverse dunes. *Prog Phys Geogr* 26:47–75

- Walker IJ, Hesp PA, Davidson-Arnott RG, Ollerhead J (2006) Topographic steering of alongshore airflow over a vegetated foredune: Greenwich dunes, prince edward island, canada. *Journal of Coastal Research* 22:1278–1291
- Walker IJ, Hesp PA, Davidson-Arnott RG, Bauer BO, Namikas SL, Ollerhead J (2009) Responses of three-dimensional flow to variations in the angle of incident wind and profile form of dunes: Greenwich dunes, prince edward island, canada. *Geomorphology* 105:127–138
- Walmsley JL, Salmon J, Taylor P (1982) On the application of a model of boundary-layer flow over low hills to real terrain. *Boundary-Layer Meteorol* 23:17–46
- Weaver C, Wiggs G (2011) Field measurements of mean and turbulent airflow over a barchan sand dune. *Geomorphology* 128:32–41
- Werner BT, Kocurek G (1999) Bedform spacing from defect dynamics. *Geology* 27:727–730
- Wiggs G, Bullard J, Garvey B, Castro I (2002) Interactions between airflow and valley topography with implications for aeolian sediment transport. *Physical Geography* 23:366–380
- Wood N (2000) Wind flow over complex terrain: a historical perspective and the prospect for large-eddy modelling. *Boundary-Layer Meteorol* 96:11–32
- Zhang C, Li Q, Zhou N, Zhang J, Kang L, Shen Y, Jia W (2016) Field observations of wind profiles and sand fluxes above the windward slope of a sand dune before and after the establishment of semi-buried straw checkerboard barriers. *Aeolian Res* 20:59–70
- Zilker DP, Hanratty TJ (1979) Influence of the amplitude of a solid wavy wall on a turbulent flow. part 2. separated flows. *J Fluid Mech* 90:257–271
- Zilker DP, Cook GW, Hanratty TJ (1977) Influence of the amplitude of a solid wavy wall on a turbulent flow. part 1. non-separated flows. *J Fluid Mech* 82:29–51

889 **Local wind regime induced by giant linear dunes**
 890 — Supplementary Material —

891 **C. Gadal*** · P. Delorme · C. Narteau · G.F.S. Wiggs · M. Baddock ·
 892 J.M. Nield · P. Claudin

893
 894 * Institut de Mécanique des Fluides de Toulouse, Université de Toulouse Paul
 895 Sabatier, CNRS, Toulouse INP-ENSEEIHT, Toulouse, France.
 896 cyril.gadal@imft.fr

897 **1. Shear velocity and calibration of the hydrodynamical roughness**

898 As the regionally predicted and locally measured velocities are available at
 899 different heights, we can not compare them directly. We therefore convert
 900 all velocities into shear velocities u_* , characteristic the turbulent logarithmic
 901 velocity profile (Spalding 1961; Stull 1988):

$$\frac{u(z)}{u_*} = \frac{1}{\kappa} \ln \left(\frac{z}{z_0} \right), \quad (15)$$

902 where z is the vertical coordinate, $\kappa = 0.4$ the von Kármán constant and z_0 the
 903 hydrodynamic roughness. Note that, strickly speaking, this logarithmic profile
 904 is valid for a neutrally stratified ABL only. Vertical density gradients occurring
 905 in other conditions may thus induce large discrepancies (Monin and Obukhov
 906 1954; Garratt 1994; Dyer 1974). However, as our wind measurements are in
 907 the flow region close enough to the surface, where these effects are negligible,
 908 this logarithmic wind profile remains a fairly good approximation in all conditions
 909 (Gunn et al. 2021b). Several measurements of hydrodynamic roughnesses
 910 are available (Raupach 1992; Bauer et al. 1992; Brown et al. 2008; Nield et al.
 911 2014). In the absence of sediment transport, it is governed by the geometric
 912 features of the bed (Flack and Schultz 2010; Pelletier and Field 2016). When
 913 aeolian saltation occurs, it is rather controlled by the altitude of Bagnold's
 914 focal point (Durán et al. 2011; Valance et al. 2015), which depends on the
 915 wind velocity and grain properties (Sherman and Farrell 2008; Zhang et al.
 916 2016; Field and Pelletier 2018). Whether associated with geometric features
 917 or with sediment transport, its typical order of magnitude is the millimetre
 918 scale on sandy surfaces.

919 We do not have precise velocity vertical profiles to be able to deduce an
 920 accurate value of z_0 in the various environments of the meteorological stations
 921 (vegetated, arid, sandy). Our approach is to rather select the hydrodynamic
 922 roughness which allows for the best possible matching between the regionally
 923 predicted and locally measured winds, i.e. minimising the relative difference δ
 924 between the wind vectors of both datasets:

$$\delta = \frac{\sqrt{\langle \| \mathbf{u}_{*,\text{era}} - \mathbf{u}_{*,\text{station}} \|^2 \rangle}}{\sqrt{\langle \| \mathbf{u}_{*,\text{era}} \|^2 \rangle \langle \| \mathbf{u}_{*,\text{station}} \|^2 \rangle}}, \quad (16)$$

where $\langle \cdot \rangle$ denotes time average. This parameter is computed for values of z_0 in ERA5-Land analysis ranging from 10^{-5} m to 10^{-2} m for the four different stations. Note that for the North Sand Sea and South Sand Sea stations, where the giant dunes feedback presumably affect the wind, we take into account the non-deflected winds only in the calculation of δ (with a 15° tolerance).

As shown in Online Resource Fig. S3, the minimum values of δ in the space $(z_0^{\text{ERA5Land}}, z_0^{\text{local}})$ form a line. We thus set the roughness in the ERA5-Land analysis to the typical value $z_0 = 10^{-3}$ m, and deduce the corresponding ones for the local stations. It leads to 2.7, 0.8, 0.1 and 0.5 mm for the Etosha West, North Sand Sea, Huab and South Sand Sea stations, respectively. Importantly, this approach somewhat impacts the calculation of the shear velocities, but not that of the wind directions. As such, most of our conclusions are independent of such a choice. However, it may affect the magnitude of the wind velocity attenuation/amplification in flow confinement situations.

2. Computation of the ABL characteristics

The estimation of the non-dimensional numbers associated with the ABL requires the computation of representative meteorological quantities. In arid areas, the vertical structure of the atmosphere can be approximated by a well mixed convective boundary layer of height H , topped by the stratified free atmosphere (Stull 1988; Shao 2008). In this context, one usually introduces the virtual potential temperature T_{vp} , which is a constant T_0 inside the boundary layer, and increases linearly in the FA (Online Resource Fig. S8a):

$$T_{\text{vp}}(z) = \begin{cases} T_0 & \text{for } z \leq H, \\ T_0 \left(1 + \frac{\Delta T_{\text{vp}}}{T_0} + \frac{N^2}{g}(z - H) \right) & \text{for } z \geq H, \end{cases} \quad (17)$$

where ΔT_{vp} is the temperature discontinuity at the capping layer and $N = \sqrt{g\partial_z T_{\text{vp}}/T_0}$ is the Brunt-Väisälä frequency, characteristic of the stratification. Note that, under the usual Boussinesq approximation, temperature and air density variations are simply related by $\delta T_{\text{vp}}/T_0 \simeq -\delta\rho/\rho_0$ (see Online Resource of Andreotti et al. (2009)), so that N can equivalently be defined from the density gradient as next to (1).

The ERA5 dataset provides vertical profiles of the geopotential ϕ , the actual temperature T and the specific humidity η at given pressure levels P . The vertical coordinate is then calculated as:

$$z = \frac{\phi R_t}{g R_t - \phi}, \quad (18)$$

where $R_t = 6371229$ m is the reference Earth radius and $g = 9.81$ m s $^{-2}$ is the gravitational acceleration. One also computes the virtual potential temperature as:

$$T_{\text{vp}} = T \left[1 + \left(\frac{M_d}{M_w} - 1 \right) \eta \right] \left(\frac{P_0}{P} \right)^{R/C_p}, \quad (19)$$

where $P_0 = 10^5$ Pa is the standard pressure, $R = 8.31$ J/K is the ideal gas constant, $C_p \simeq 29.1$ J/K is the air molar heat capacity, and $M_w = 0.018$ kg/Mol and $M_d = 0.029$ kg/Mol are the molecular masses of water and dry air respectively. The specific humidity is related to the vapour pressure p_w as

$$\eta = \frac{\frac{M_w}{M_d} p_w}{p - \left(1 - \frac{M_w}{M_d}\right) p_w}. \quad (20)$$

The ERA5 dataset also provides an estimate of the ABL depth H , based on the behaviour of the Richardson vertical profile. This dimensionless number is defined as the ratio of buoyancy and flow shear terms, and can be expressed as $\text{Ri} = N^2 / (\partial_z u)^2$. It vanishes in the lower well-mixed layer where T_{vp} is constant, and increases in the stratified FA. Following the method and calibration of Vogelegang and Holtlag (1996); Seidel et al. (2012), the value $\text{Ri}(z) \simeq 0.25$ has been shown to be a good empirical criterion to give $z \simeq H$ within a precision varying from 50% for the shallower ABL (e.g. at night) to 20% for situations of stronger convection.

Examples of vertical profiles of the virtual potential temperature deduced from ERA5 are shown in Online Resource Fig. S8a. For each of them, an average temperature is computed below the ABL depth ($z < H$), and a linear function is fitted above, allowing us to extract the temperature jump ΔT_{vp} . Importantly, some profiles display a vertical structure that cannot be approximated by the simple form (17) used here (Online Resource Fig. S8b). In practice, we removed from the analysis all of those leading to the unphysical case $\Delta T_{\text{vp}} < 0$. We have noticed that these ‘ill-processed’ profiles dominantly occur in winter and are evenly spread across the hours of the day. Importantly, they represent $\simeq 12\%$ of the data only (Online Resource Fig. S8c,d), and we are thus confident that this data treatment does not affect our conclusions.

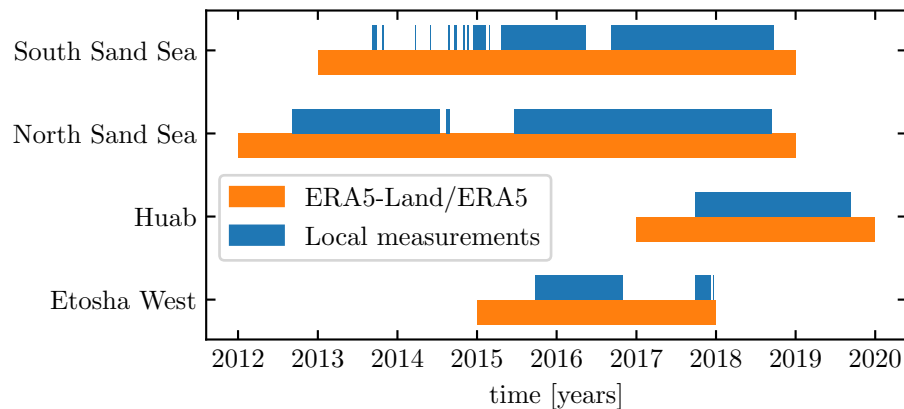


Fig. S1 Gant chart representing the valid time steps for the two data sets, for all stations.

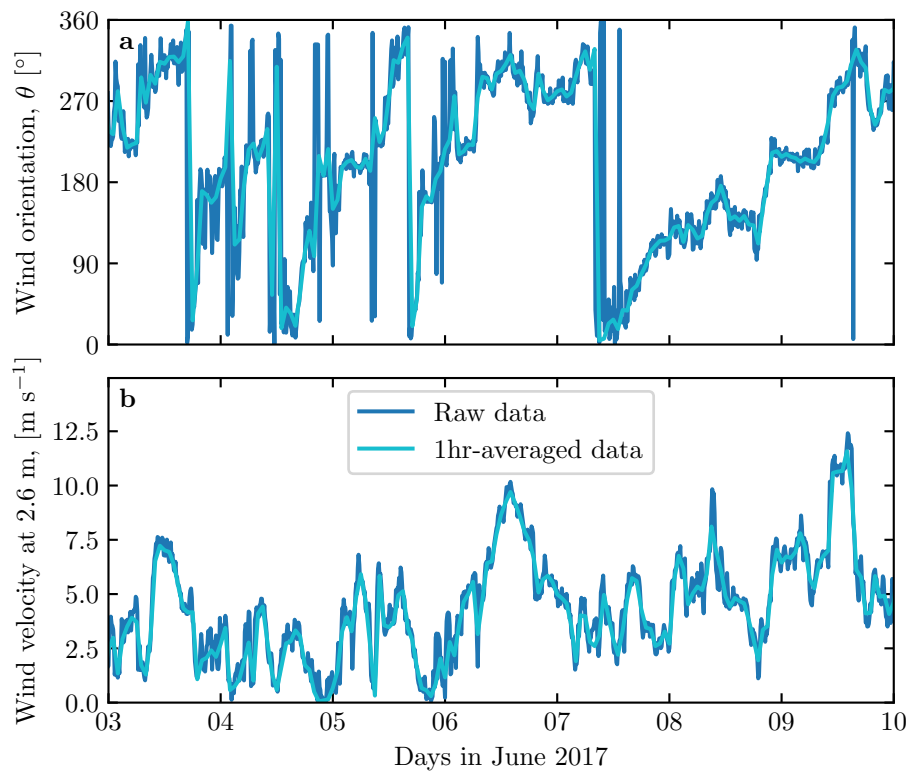


Fig. S2 Local wind measurements: comparison between raw (blue) and hourly-averaged (light blue) data from South Sand Sea station. **a:** wind direction. **b:** wind velocity at height 2.6 m.

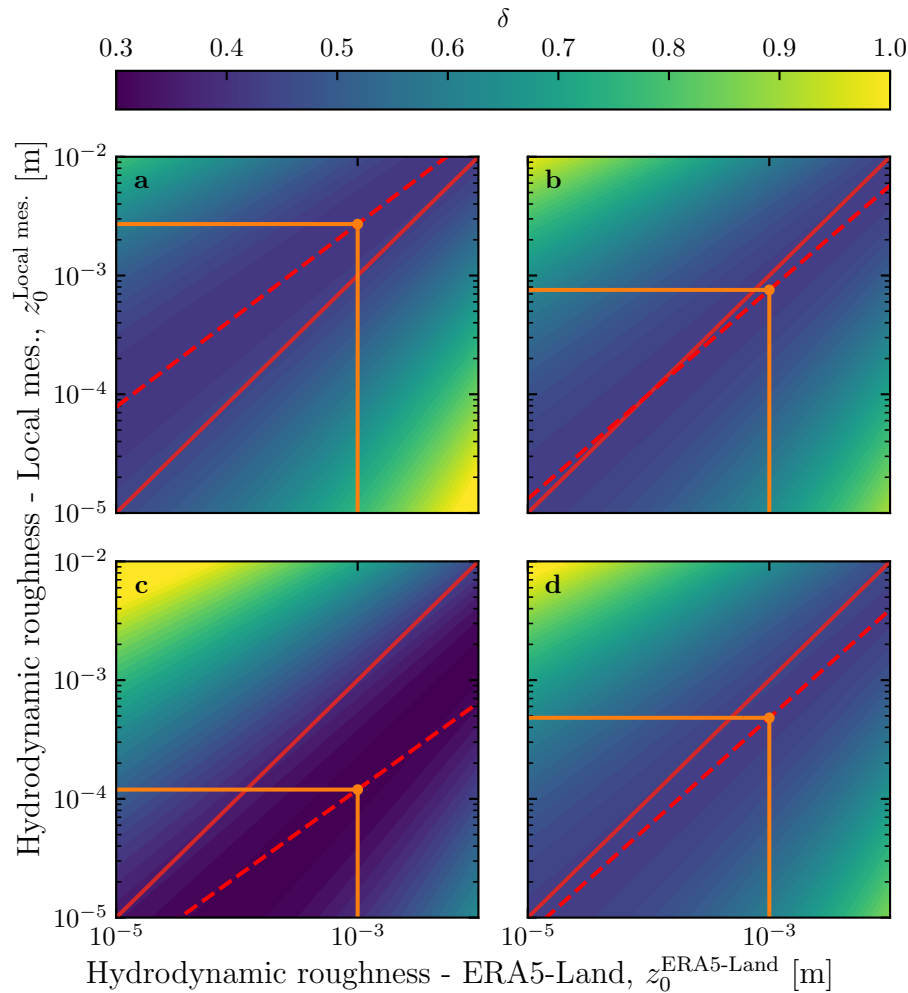


Fig. S3 Calibration of hydrodynamic roughness. The parameter δ (16) quantifying the difference between local and predicted winds is shown in color scale as a function of the hydrodynamic roughnesses chosen for the ERA5-Land and for local winds, for the (a) Etosha West, (b) North Sand Sea, (c) Huab and (d) South Sand Sea stations. The red dashed and plain lines shows the minima of δ and the identity line, respectively. The orange lines and dots highlight the chosen hydrodynamic roughnesses for the local winds deduced from setting $z_0^{\text{ERA5-Land}} = 1 \text{ mm}$.

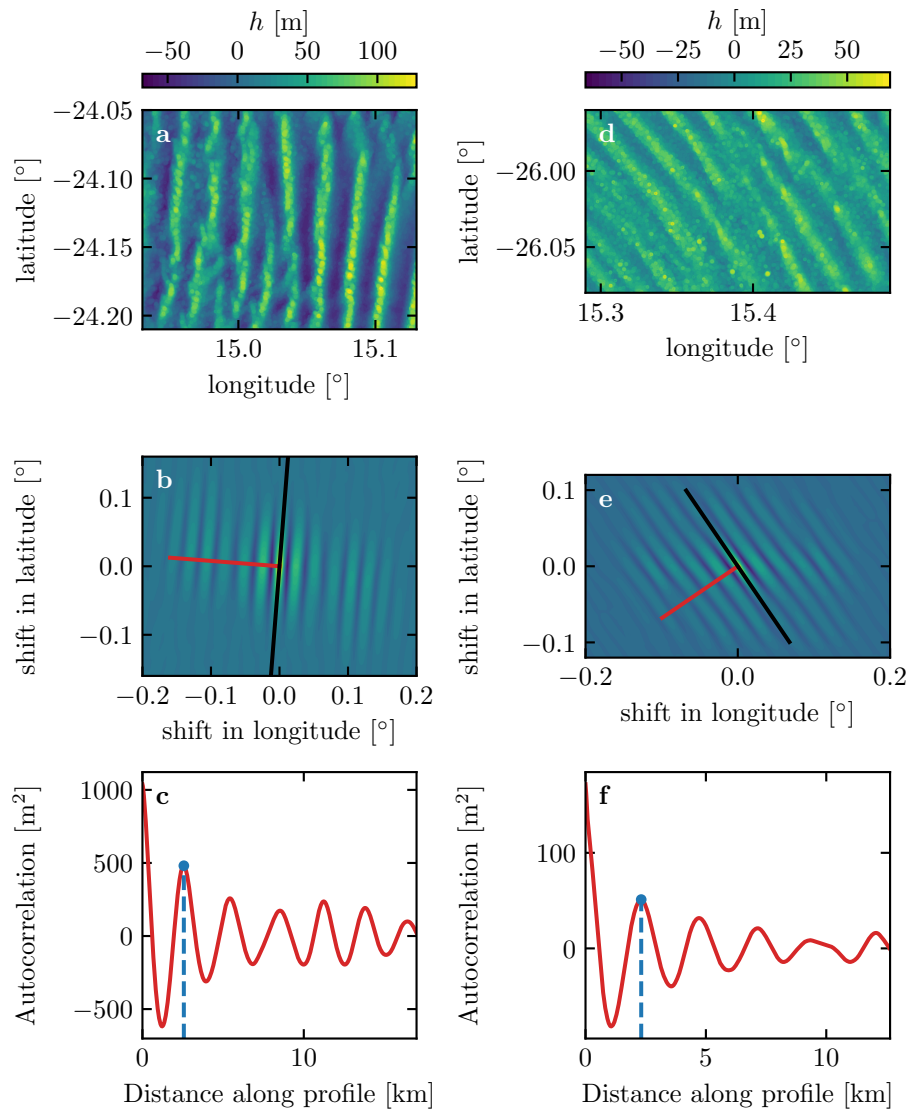


Fig. S4 Analysis of the DEMs of the North Sand Sea (left column – panels **a**, **b**, **c**) and South Sand Sea (right column – panels **d**, **e**, **f**) stations. **a–d**: Bed elevation detrended by a fitted second order polynomial base-line. **b–e**: Autocorrelation matrix shown in color scale. The black line shows the detected dune orientation, and the red line represents the autocorrelation profile along which the dune wavelength is calculated, displayed in **c–f**. The blue lines and dots show the first peak of the autocorrelation profile, whose abscissa gives the characteristic wavelength of the dune pattern.

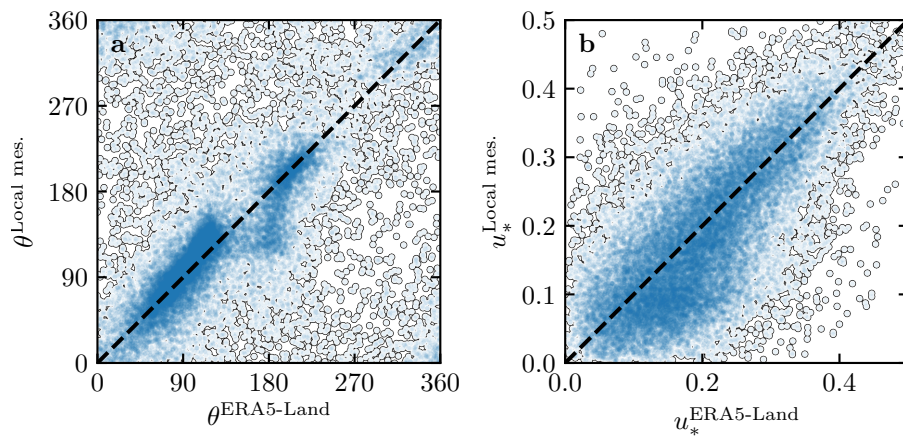


Fig. S5 Statistical comparison of the wind orientation (a) and velocity (b) between the ERA5-Land dataset and the local measurements for the Huab and Etosha West stations. Data point clustering around identity lines (dashed and black) provide evidence for agreement of the two sets.

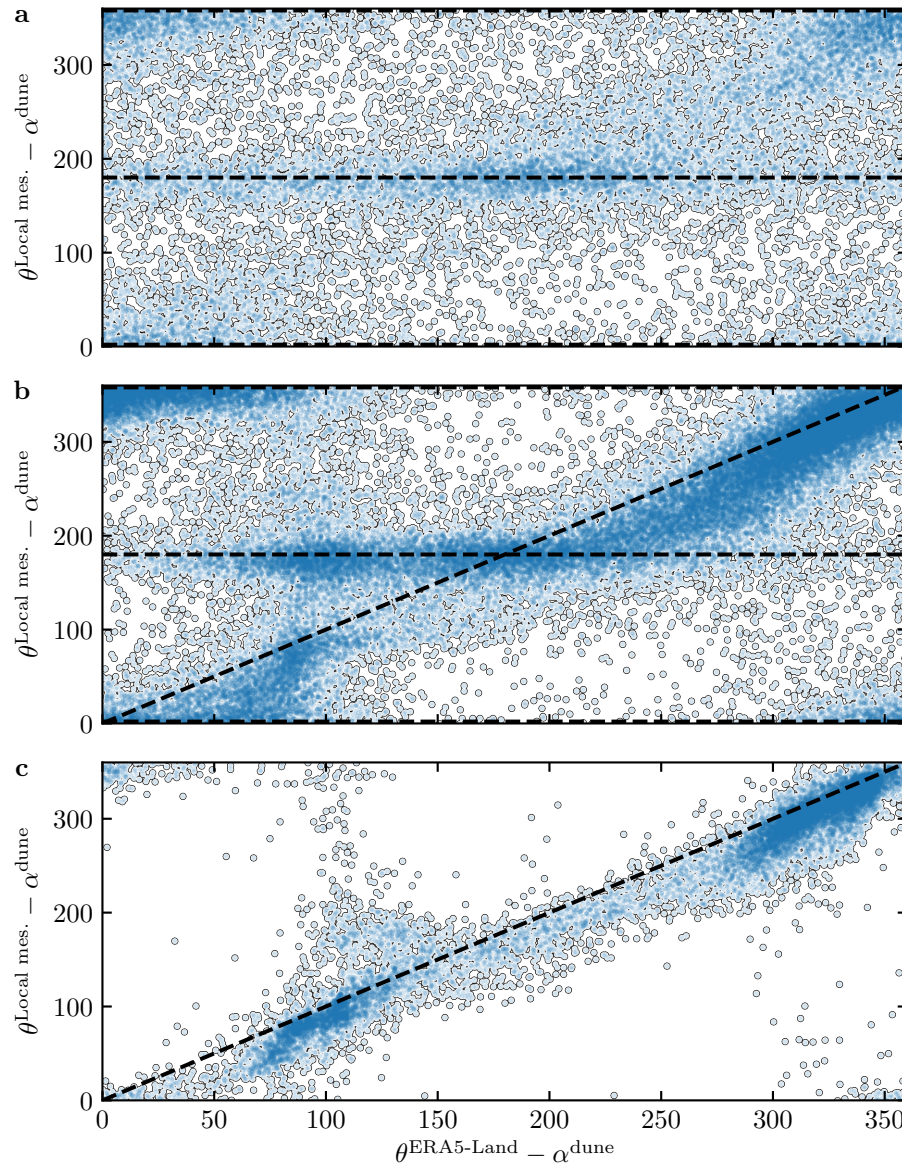


Fig. S6 Statistical comparison of the wind orientation between the ERA5-Land dataset and the local measurements for the South Sand Sea and North Sand Sea stations, for different velocity ranges. **a:** $u^{\text{ERA5-Land}}_* < 0.1 \text{ m s}^{-1}$. **b:** $0.1 < u^{\text{ERA5-Land}}_* \leq 0.25 \text{ m s}^{-1}$. **c:** $u^{\text{ERA5-Land}}_* \geq 0.25 \text{ m s}^{-1}$. The measured dune orientations are subtracted to the wind orientation, which allows us to plot both stations on the same graph. Black dashed lines indicate locally measured orientations aligned with the dune crests (here 0° , 180° and 360° – panels **a**, **b**), as well as the identity lines (panels **b**, **c**).

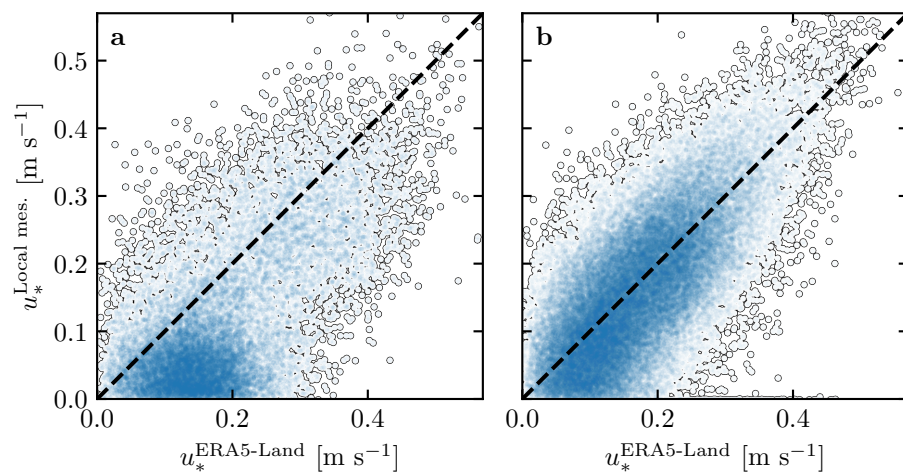


Fig. S7 Statistical comparison of the wind velocity between the ERA5-Land dataset and the local measurements for the South Sand Sea and North Sand Sea stations. **a:** Nocturnal summer easterly wind. **b:** Diurnal southerly wind. Black dashed lines are identity lines. The angle ranges used to select diurnal and nocturnal summer winds are the same as those in Figs. 4 and Figs. 6 of the main article.

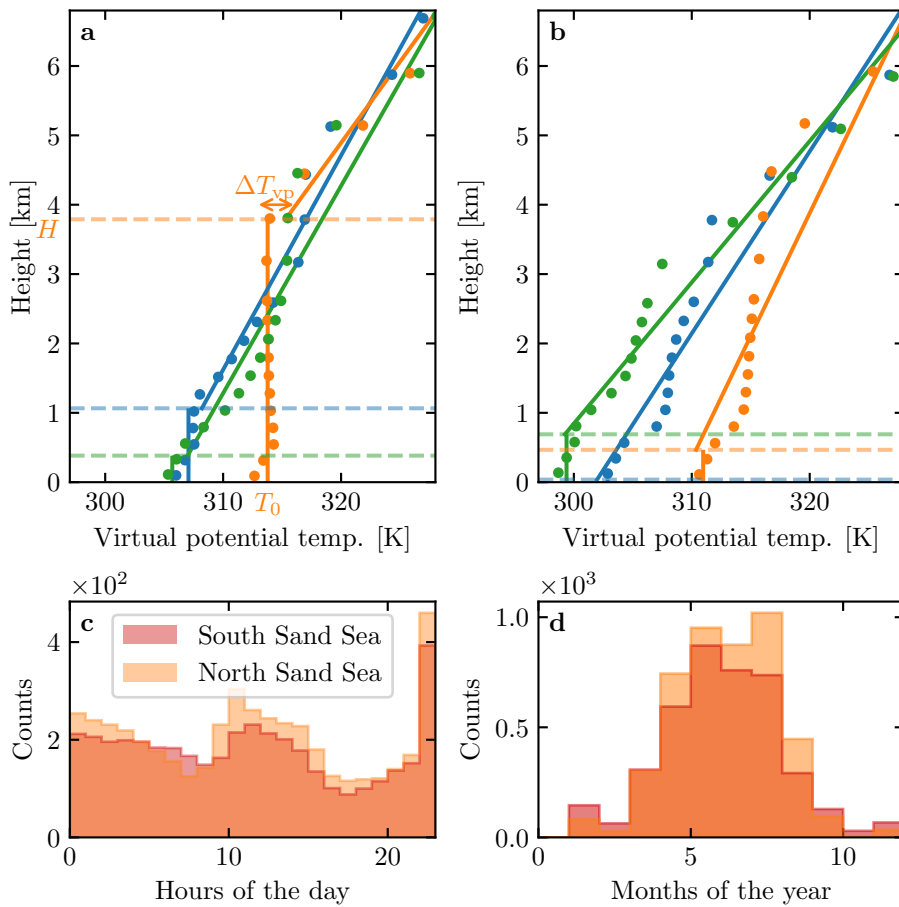


Fig. S8 **a:** Vertical profiles of the virtual potential temperature at three different times (blue: 29/11/2012 - 11.00 UTC, orange: 21/03/2017 - 12.00 UTC, green: 21/03/2017 - 20.00 UTC) at the South Sand Sea station. Dots: data from the ERA5 reanalysis. Dashed lines: boundary layer height given by the ERA5 reanalysis. Plain lines: vertical (ABL) and linear (FA) fits to estimate the quantities displayed in Online Resource Fig. S9. **b:** Examples of ill-processed vertical profiles at three different times (blue: 2/12/2013 - 23.00 UTC, orange: 20/03/2017 - 00.00 UTC, green: 14/07/2017 - 14.00 UTC) at the South Sand Sea station. Distribution of ill-processed vertical profiles at South (orange) and North (light orange) Sand Sea station: hourly **(c)** and monthly **(d)** counts.

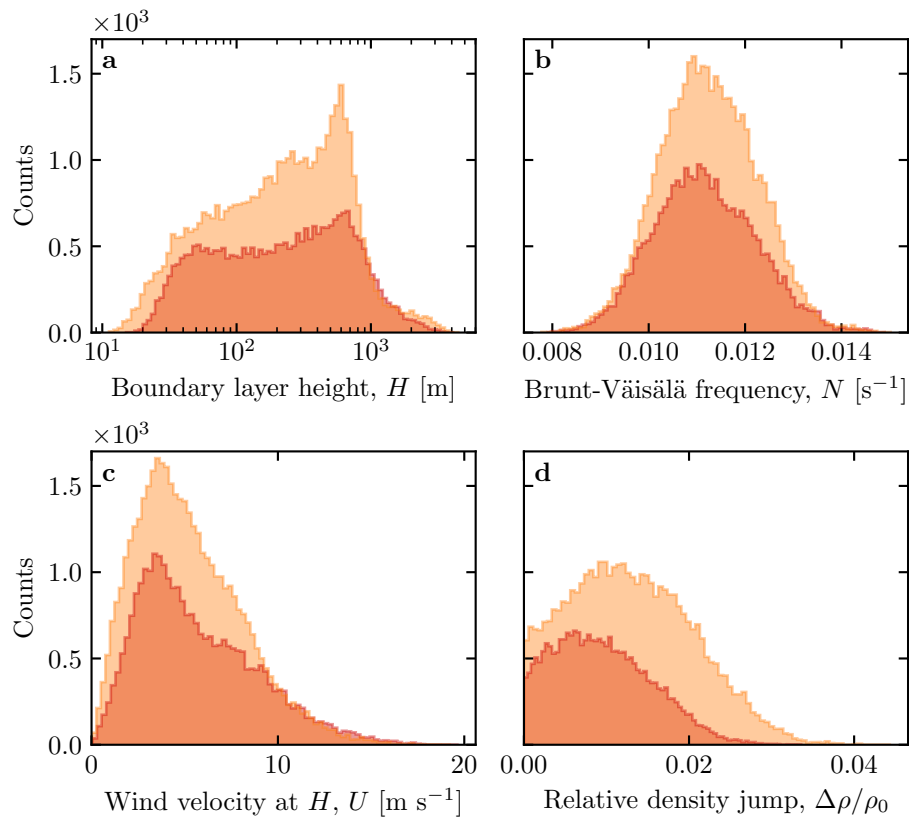


Fig. S9 Distributions of the meteorological parameters resulting from the processing of the ERA5-Land data for the South Sand Sea (orange) and the North Sand Sea (light orange) stations.

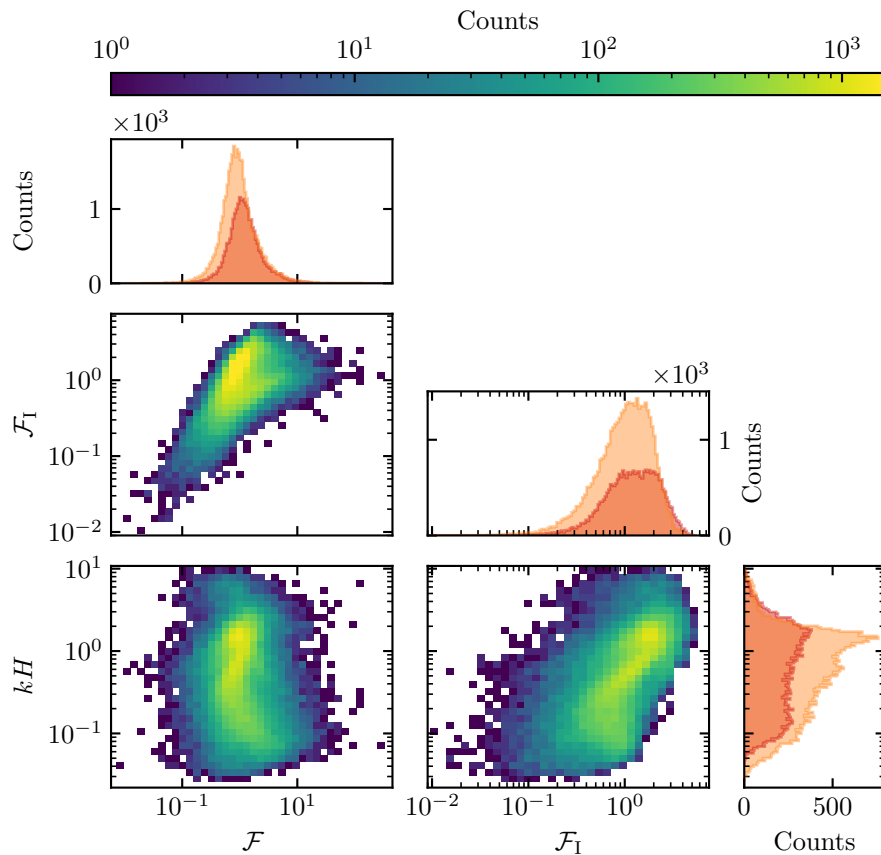


Fig. S10 Non-dimensional parameters distributions. For the marginal distributions, the light orange corresponds to the South Sand Sea station, and the orange to the North Sand Sea station.

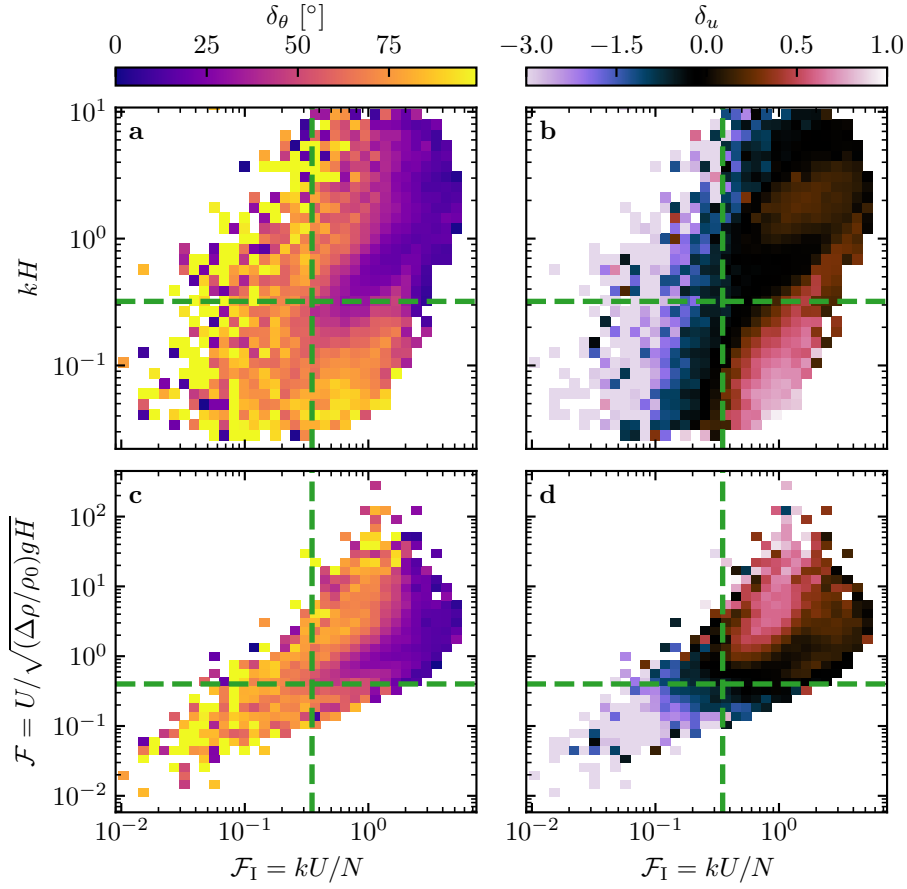


Fig. S11 Regime diagrams of the wind deviation δ_θ and relative attenuation/amplification δ_u in the spaces (\mathcal{F}_I, kH) and $(\mathcal{F}_I, \mathcal{F})$, containing the data from both the North Sand Sea and South Sand Sea stations. Green dashed lines empirically delimit the different regimes. The point density in each bin of the diagrams is shown in Online Resource Fig. S10 – 95% of the data occur in the range $-1 < \delta u < 1$. The similar regime diagrams in the space (\mathcal{F}, kH) are shown in Fig. 8.

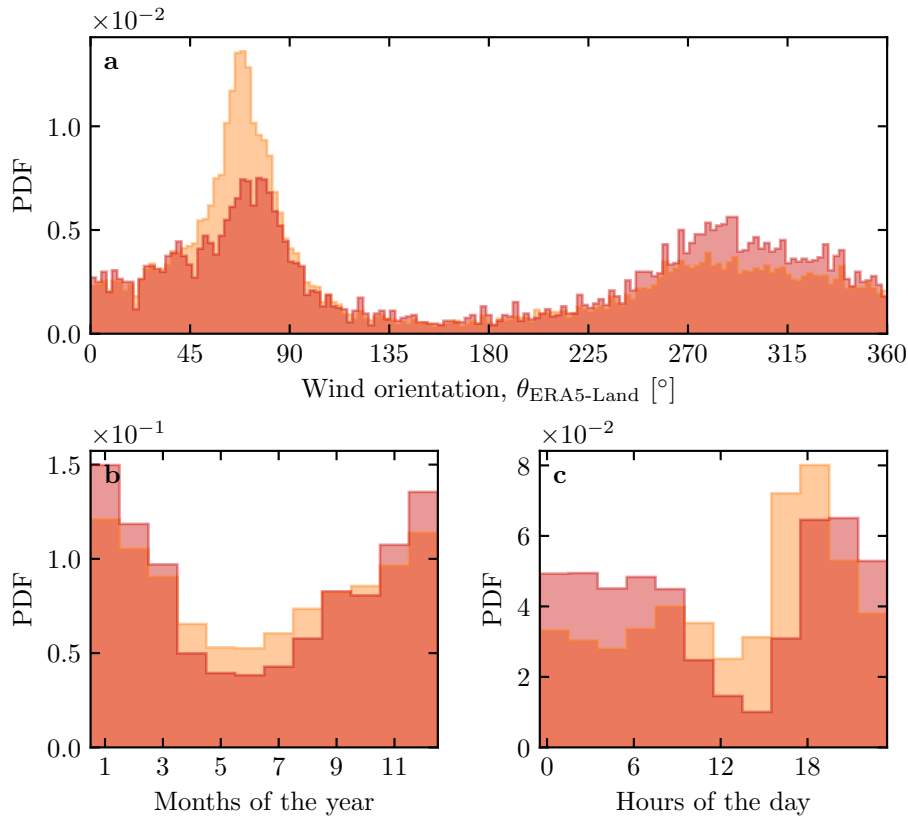


Fig. S12 Normalized distributions of amplified velocities for the North sand Sea (light orange: $\delta_u < 0$, orange: $\delta_u < -0.5$). **a:** Angular distributions. **b:** Monthly distributions. **c:** Hourly distributions.

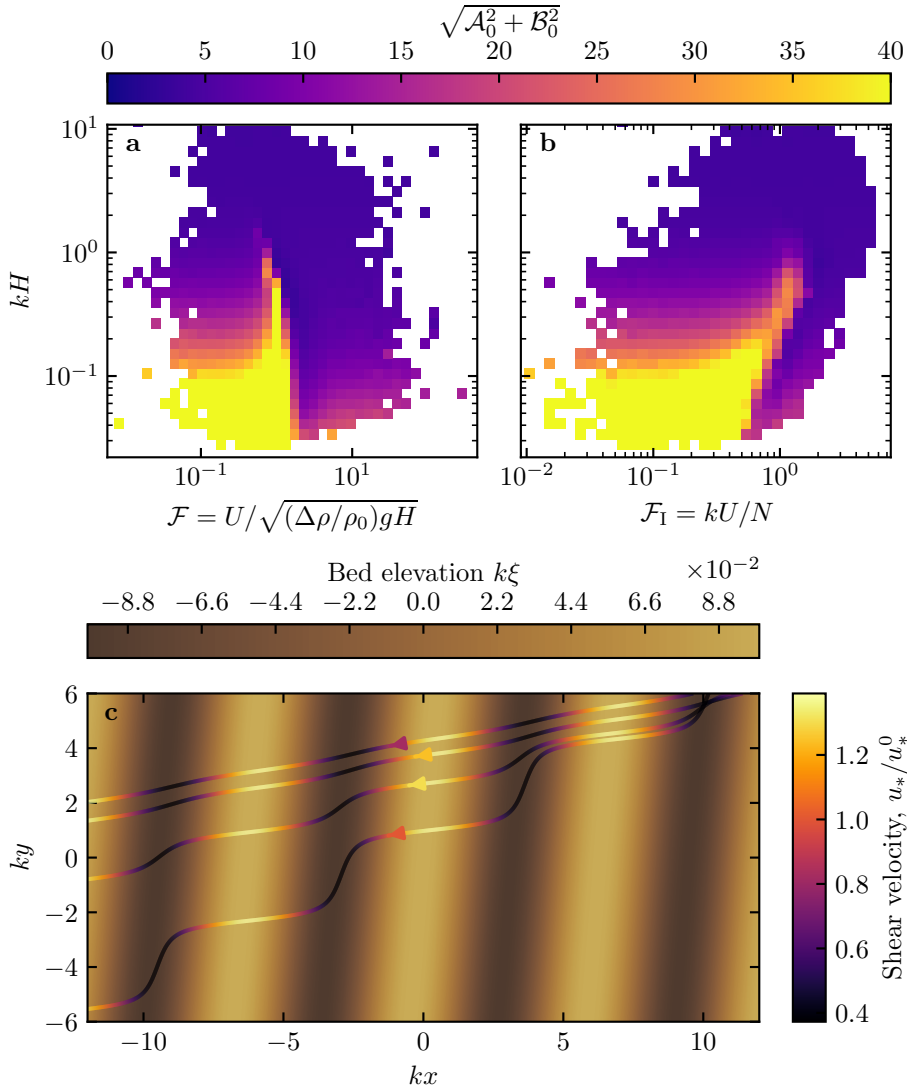


Fig. S13 Computation of the flow disturbance with the linear model of Andreotti et al. (2009). **a–b:** Magnitude of the hydrodynamic coefficients A_0 and B_0 , calculated from the time series of the non-dimensional numbers corresponding to the ERA5-Land wind data and ERA5 data on vertical pressure levels. **c** Shear velocity streamlines over sinusoidal ridges of amplitude $k\xi_0 = 0.1$ and for increasing values of $\sqrt{A_0^2 + B_0^2}$. From the upper to the lower streamline, values of $(kH, \mathcal{F}, \mathcal{F}_I, A_0, B_0, \sqrt{A_0^2 + B_0^2})$ are $(1.9, 0.6, 1.5, 3.4, 1.0, 3.5)$, $(1.5, 0.3, 0.4, 4.8, 1.4, 5.0)$, $(0.1, 3.5, 1.0, 8.6, 0.1, 8.6)$, $(0.5, 0.05, 0.04, 9.6, 2.5, 9.9)$.

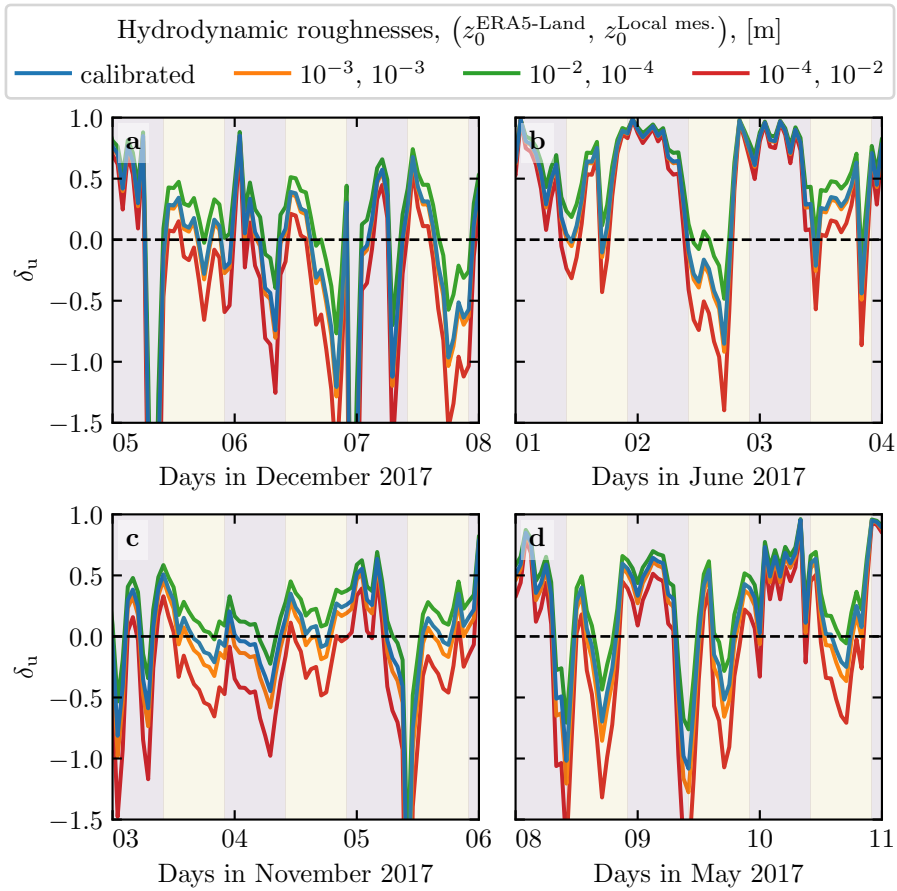


Fig. S14 Time series of the relative velocity disturbance δ_u corresponding to Fig. 5, for different values of the hydrodynamic roughnesses. **a:** North Sand Sea – summer, **b:** North Sand Sea – winter, **c:** South Sand Sea – summer, **d:** South Sand Sea – winter. Note that δ_θ is independent of the choice of $z_0^{\text{ERA5-Land}}$ and $z_0^{\text{Local mes.}}$.